UNIVERSITY OF CALIFORNIA,

IRVINE

Ultrafast Photo-induced Force Microscopy

THESIS

Submitted in partial satisfaction of the requirements

for the degree of

DOCTOR OF PHILOSOPHY

in Physics

by

Jordan Brocious

Thesis Committee:
Professor Eric O. Potma, Chair
Professor Wilson Ho
Professor Ilya Krivorotov

2014

Table of Contents

	Page
List of Figures	**v**
Acknowledgments	**vii**
Abstract of the Thesis	**viii**
1 Introduction	
1.1 Optical Microscopy and the Diffraction Limit	**1**
1.2 Atomic Force Microscopy and Material Characterization	**4**
1.3 Combined Techniques and Optical Force Microscopy	**6**
2 Photo-induced Force Theory	
2.1 Optical Force Interactions at the Tip	**10**
2.2 Gradient Force	**12**
2.3 Scattering Force	**14**
2.4 Cantilever Dynamics	**16**
2.5 Reconstruction of Interaction Forces	**18**
3 Experimental	
3.1 Experimental Apparatus	**21**
3.2 Sample Materials	**26**
4 Results and Discussion	
4.1 Force-distance Simulations	**29**
4.2 Photo-induced Forces Near Gold Nanowires	**32**
4.3 Photo-induced Forces and Molecular Resonances	**36**
5 Pump-probe Force Microscopy	
5.1 Introduction	**41**
5.2 Pump-probe Basics and Nonlinear Optical Spectroscopy	**43**
5.3 Pump-probe Optical Microscopy of SiNc	**48**
5.4 Nonlinear Ultrafast Photo-induced Force Microscopy	**55**

5.5 Time-resolved Pump-probe Force Microscopy **61**

6 Conclusion

6.1 Summary **65**

Bibliography **68**

List of Figures

		Page
1.1	Diffraction Limit	2
1.2	Photo-induced Force Microscopy Illustration	8
2.1	Induced Dipole Diagram	11
2.2	Cantilever-tip Motion	16
3.1	Photo-induced Force	23
3.2	Microscopy System	25
3.3	Electric Field Intensity Distribution	26
3.4	Photo-induced Force Interaction Over the Focal Field	28
4.1	Chemical Structure and Absorption Spectrum of SiNc	30
4.2	Amplitude and Phase Simulations of Cantilever Dynamics	32
4.3	Independence of Bulk Thickness on PIFM	33
4.4	Photo-induced Force-distance Curves of Gold Nanowire	35
4.5	Photo-induced Force Microscopy of SiNc Nanoclusters	36
4.6	Photo-induced Force-distance Curves of SiNc	38
4.7	Reconstructed Optical Force-distance Curves Comparison	39
5.1	Pump-probe basics	44
5.2	Linear absorption of SiNc in solution and glass slide	46
5.3	Excited state absorption spectrum of SiNc	48

5.4 Schematic of optical pump-probe microscope 49

5.5 Nonlinear optical imaging of SiNc clusters 51

5.6 Time-resolved excited state absorption images of SiNc cluster 52

5.7 Excited state absorption decay dynamics 53

5.8 Further decay dynamics of SiNc 54

5.9 Photo-induced microscope for nonlinear processes 55

5.10 Tip-scan of nonlinear interaction 58

5.11 Pump-probe force microscopy images of SiNc nanoclusters 59

5.12 Pump-probe force microscopy enhanced contrast over topography 61

5.13 Time-resolved pump-probe force microscopy of SiNc 63

5.14 Comparison of time-resolved excited state dynamics measurements 64

Acknowledgments

I must express deep gratitude for my advisor, Professor Eric Potma, for supporting me throughout these difficult experiments. I must truly thank Junghoon Jahng and Dr. Dmitry Fishman for their scientific acumen, hard work, and generosity in the creation of this work. I would like to thank my collaborating advisor Professor H. Kumar Wickramasinghe and his team Fei Huang, Venkata Ananth Tamma, and Dr. Jon Burdett for their contributions and fruitful association. Thanks to Xiaowei Li for the nanowire fabrication. I would like to thank Dr. Tatyana Sheps and especially Dr. Desiré Whitmore for their mentorship.

This work funded by the National Science Foundation Chemistry at the Space-Time Limit (CaSTL) center, and I thank them for the support and collaborative environment.

On a personal level I would like to thank everyone who passed through The Compound for all the love and support. And thanks to the Radical Student Union and Take Back UCI crews for all that you did

Abstract of the Thesis

Ultrafast Photo-induced Force Microscopy

By

Jordan Brocious

Doctor of Philosophy in Physics

University of California, Irvine, 2014

Professor Eric O. Potma Irvine, Chair

Photo-induced force microscopy is a novel technique where mechanical detection with a cantilevered probe replaces the detection of photons to investigate optically induced processes and states. A theoretical and experimental analysis is performed here of the forces present in photo-induced force microscopy operated in tapping mode, which reveals two dominant optically induced forces, the gradient force and the scattering force. Force-distance curves are reconstructed from experimental amplitude and phase information for glass, gold nanowires and molecular clusters of silicon naphtalocyanine samples. The scattering force is shown to be insensitive to both nano-scale tip-sample distances and sample polarizability and is dependent on the form of the tip. The gradient force demonstrates a z^{-4} tip-sample distance dependence, localized to a few nanometers, and is strongly dependent on the polarizability of the sample which

enables spectroscopic imaging through force detection. The different distance-dependence and polarizability-dependence of the gradient and scattering forces give rise to a complex force-distance curve which determines imaging contrast along with the cantilever set-point, knowledge of which is essential for image interpretation.

Photoinduced force microscopy is then extended to ultrafast pump-probe measurements of the material's nonlinear polarization. It is demonstrated that the photo-induced force is sensitive to the same excited state dynamics as measured in optically-detected experiments. Ultrafast pump-probe force microscopy brings nanoscale spatial resolution with non-optical detection to time-resolved studies of excited state dynamics with sensitivities approaching the single molecule limit.

Chapter One

Introduction

1.1 Optical microscopy and the diffraction limit

The study of optically-induced processes in single molecules and nano-structures can yield vast information on the chemical world, from the identification of chemical components, the conformational changes of molecules, and the dynamics of vibrational and electronic transitions [1].

When investigating these processes through optical detection however, the spatial resolution is limited to separations larger than the diffraction limit $\frac{\lambda}{2\,NA}$, where λ is the illumination wavelength and NA is the numerical aperture of the collection optics. Being restricted to approximately half the wavelength, the spatial resolution limits the information that can be gathered from ensembles of nanoscopic systems, such as ensembles of molecules. When ensembles are probed rather than the individual, averaging over optical properties occurs, which

blurs information about conformational and transitional states of molecules. To track the dynamics of individual molecules, they have to be measured one at a time. Single molecule measurements are greatly facilitated by a higher spatial resolution, which enables the differentiation of two closely spaced molecules. Several optical techniques have been developed that allow probing of nanostructures with a resolution beyond the diffraction limit.

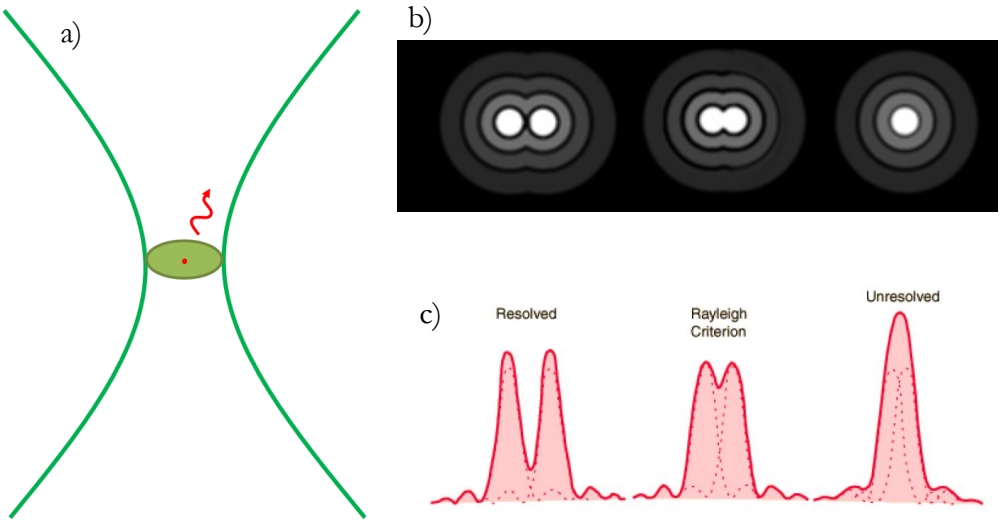

Figure 1.1: Single molecular emitter in the focal plane a) and the smearing of images b) from unresolved intensity distributions c) [2]

Fluorescence of single molecules in cryogenic and then ambient conditions has been well established with the development of single-photon detectors [3, 4]. Recently, the ability to control the density of emission of fluorophores combined with knowledge of the single-molecule position within the point-spread function of the microscope has allowed 3D imaging of labeled-biological structures with

resolution down to 20nm [5, 6]. This technique is known as single-molecule photoactivated localization microscopy (PALM) and works by gathering multiple frames of sparsely distributed fluorophores whose individual locations are determined by mathematical fitting, allowing image reconstruction with super-resolution.

Manipulating the shape of a pump laser and a second donut-shaped erasing laser can also improve resolution beyond the diffraction limit, for instance through the process of stimulated emission depletion of fluorophores in the periphery of the focal volume [7, 8].

Techniques like PALM however do not provide direct information on the optical properties of the sample in question and rely on tags to localize the structure.

To directly probe single molecules without fluorescent tags, Raman-based techniques can be used. However, the Raman effect is notoriously weak and strong amplification is needed to raise the Raman response to detectable levels. This can be accomplished by equipping molecules with plasmonic antennae. The strong plasmonic resonances in noble metals, which originate from collective oscillations of conduction electrons coupled with electromagnetic waves, can generate field enhancement up to 10^3 and surface-enhanced Raman spectroscopy (SERS) intensity enhancement factors theoretically of $\sim 10^{15}$ [9-11]. This has allowed studies of single molecule resonant Raman spectroscopy[12] and even single molecule time-resolved coherent anti-Stokes Raman spectroscopy (CARS)

using dumbbell geometry plasmonic substrates, following vibrational motions in real time [13].

Well-separated single molecules with large optical cross-sections such as carbon nanotubes have also been imaged and characterized with Raman spectroscopy, CARS, and pump-probe techniques [14, 15].

The use of optical fields for mechanical manipulation of objects, most commonly optical tweezer techniques, has advanced to the manipulation of nano-sized objects through the use of fields resonant to the object's electronic transitions [16-19]. Optical force manipulation with resolution beyond the diffraction limit has been shown with these techniques.

1.2 Atomic force microscopy and material characterization

Scanning probe techniques, however, are capable of imaging features thousands of times smaller than the optical diffraction limit. Specifically, the scanning probe technique known as atomic force microscopy (AFM), which relies on neither photons nor electrons for imaging detection, developed in 1986 by Binnig et al., has matured to the point of enabling visualization of individual atoms and intermolecular bonds [20-22]. AFM is primarily an imaging tool, generated by variations in the local forces between the cantilevered-atomically sharp tip and the sample surface.

In dynamic AFM modes, amplitude or frequency modulated, the cantilever feedback and subsequent image contrast can come from the shift in resonance frequency, phase shift, or the amplitude variation in the oscillation. Much of the image contrast used for surface topography is due to the very short range repulsion of electron orbital overlap, but through analysis of force-versus-distance curves for tip-sample separation further force interactions can be investigated and formulas for these forces can be determined from the mechanical response of the AFM [23-25]. So, while AFM is exceptional at imaging surface topography in vacuum, air, or liquid environments, it can also be used to characterize certain material properties. In phase-imaging AFM the elasticity, adhesion and friction can be determined, and by voltage-biasing the tip the electronic properties such as the dielectric constant and capacitance can be found, a technique known as electrostatic force microscopy or Kelvin probe force microscopy [24, 26, 27]. In UHV a tip coated in magnetic material can use short-range magnetic exchange force for magnetic imaging on the sub-nanometer scale [28]. Through the functionalizing of the AFM tip with particular chemical groups specific chemical fingerprinting is enabled, allowing imaging of interaction sites on single proteins or the chemical determination of a lattice [29, 30].

1.3 Combined techniques and optical force microscopy

However, the AFM, without the difficult and poorly controlled tip-functionalization, is largely insensitive to the chemical details of the sample, and there are only a few techniques which combine the spectroscopic power of optical microscopies with the spatial resolution of AFM.

By introducing an optical probe in the near-field of the sample the spatial resolution is determined by the sharpness of the probe while still retaining the spectroscopic benefits of far-field optical techniques. Localized illumination is created by a tip scanned closely over the sample, known as near-field scanning optical microscopy (NSOM). In aperture-type NSOM an optical fiber is pulled to an aperture on the order of tens of nanometers, and can be used to generate or collect evanescent fields for a resolution of 50-100 nm. However, this technique is incompatible with fs-pulses because of the spectral and temporal broadening due to the fiber [10, 31]. In apertureless NSOM (ANSOM) a much sharper tip is used and it relies on the scattering of light and the locally enhanced optical fields. However, ANSOM is more complex and less understood, though attempts have been made at a general nano-focusing theory [32]. Tip-enhanced Raman spectroscopy (TERS) in ambient conditions has been done with single-molecule specificity by comparing dilute isotopologues [33]. Nonlinear and femtosecond

tip-enhanced experiments have been carried out despite the difficulties related to high peak-power photodamage and undesirable nonlinear effects [31, 34].

Recent developments in combining light-induced molecular excitations with mechanical force detection are of particular interest, as these approaches seek to add chemical selectivity to force microscopy. Instead of relying on optical detection of the optically-induced states and interactions, these techniques use mechanical detection of the subsequent forces. This avoids some of the difficulties of optical detection, the infrequent single photons of frequency-shifted scattered light for Raman imaging or the minute changes in the probe modulation train for pump-probe techniques, and instead is detected on a separate mechanical channel, without an optical background, localized to the spatial scale near the size of the mechanical probe.

The photo-thermal induced resonance technique (or AFM-IR) uses tunable IR sources to directly excite dipole-allowed vibrational transitions producing thermal expansion, which is detected by a contact-mode AFM [35-38]. Overlapping the laser repetition rate with the first mechanical resonance of the cantilever combined with the field enhancement of the tip has allowed AFM-IR spectroscopy of single monolayers and sensitivity detection limits down to ~30 molecules [39].

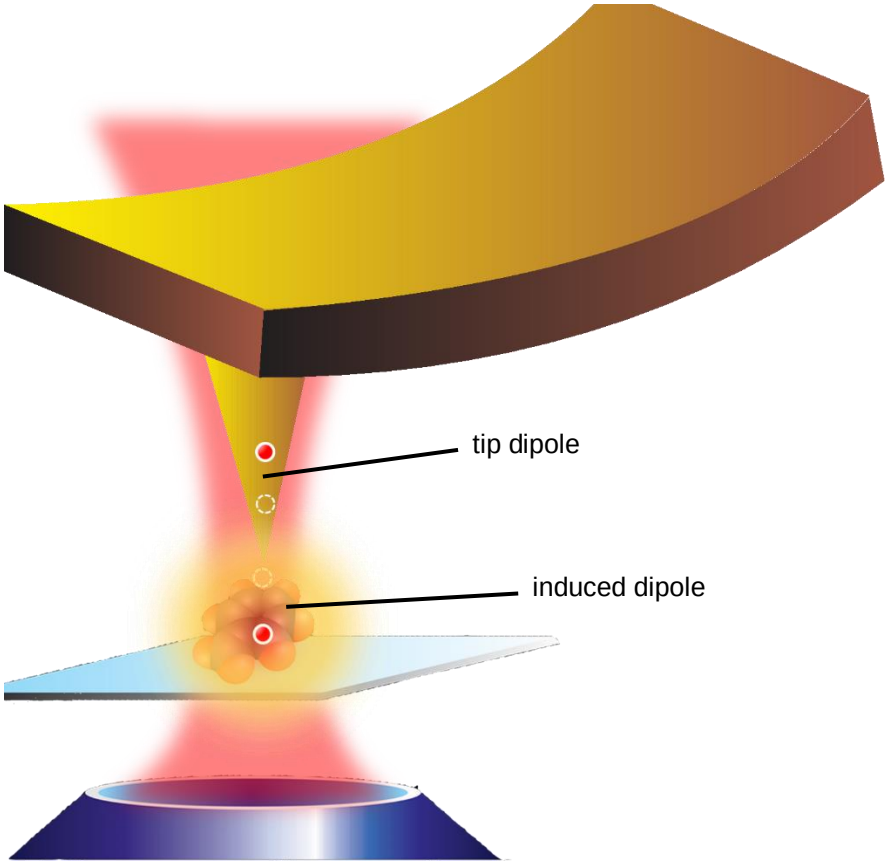

Figure 1.2: Photo-induced force microscopy illustration, where the incident field, and the induced dipole of the tip and molecule all interact, and these optically induced dipole interactions are mechanically detected by the AFM probe.

Photo-induced force microscopy is an alternative method that does not rely on thermal expansion, but instead directly probes the optically induced changes in the dipolar interactions between the polarizable AFM tip and sample, first demonstrated by the Wickramasinghe group [40]. Any optical transition, including multiphoton absorption and Raman processes, may introduce a change in the local interaction force, which can in turn be measured via the cantilever deflection. This technique is not restricted to contact-mode as in AFM-IR and

can gain the benefits of dynamic-mode operation. It is also advantageous to directly probe optical transitions without relying on energy dissipation and subsequent thermal expansion in the sample. Theoretically, the spectroscopic information probed in this technique is similar to information accessible through coherent optical spectroscopy with heterodyne detection [41]. Pump-probe processes can be observed without optical background, and since the optically-induced forces are spatially confined to the probe tip and excitation dipole dimensions, the spatial resolution is improved beyond TERS and AFM-IR, with near-field detection and decoupled from heat diffusion, ~4nm [42].

The current theoretical treatment of the relevant forces in the tip-sample junction is inadequate to develop Photo-induced force microscopy. Here we will consider the attractive gradient interactions and the repulsive scattering force in terms of classical fields and forces, for a simple description of the operating principle of the technique. Through the simulation and experimental comparison of the force-distance curves we identify the distances regimes in which the attractive gradient force are dominant and where chemically selective signals are optimized.

Chapter Two

Photo-induced Force Theory

2.1 Optical Force Interactions at the Tip

To begin to develop a theory of the optical force interactions at the AFM tip, we first consider a polarizable particle illuminated with a monochromatic electromagnetic wave, of angular frequency ω, where the time harmonic electric and magnetic field components at location $\mathbf{r}$ can be described by:

$$\mathbf{E}(\mathbf{r},t) = \mathrm{Re}[\mathbf{E}(\mathbf{r})e^{-i\omega t}] \tag{2.1}$$

$$\mathbf{B}(\mathbf{r},t) = \mathrm{Re}[\mathbf{B}(\mathbf{r})e^{-i\omega t}] \tag{2.2}$$

The particle then acquires an induced dipole moment with the same time dependence as the incident fields, and can be written as:

$$\vec{\mu}(\mathbf{r},t) = \mathrm{Re}[\vec{\mu}(\mathbf{r})e^{-i\omega t}] \tag{2.3}$$

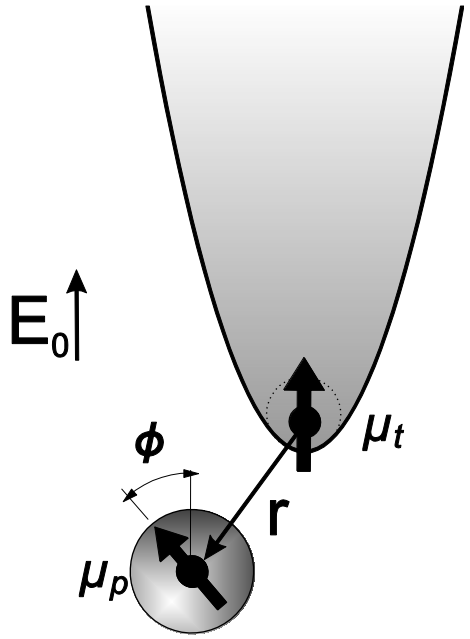

Figure 2.1: Induced dipole moments of an AFM tip and particle with incident electromagnetic field, where **r** is the center of mass coordinate

Assuming the particle has no static dipole moment of its own, the induced dipole moment, to the first order, is proportional to the electric field at the particle position **r** given as:

$$\vec{\mu}(\mathbf{r}) = \alpha(\omega)\mathbf{E}(\mathbf{r}) \tag{2.4}$$

where α denotes the polarizability of a particle that satisfies the Clausius-Mossotti relation

$$\alpha = 4\pi\epsilon_0\left(\frac{\epsilon - 1}{\epsilon + 2}\right)a^3 \tag{2.5}$$

where *a* is the particle radius and ϵ denotes the complex dielectric permittivity. For particles such as single molecules the projection of $\vec{\mu}$ along the direction of

the magnetic field is the only relevant component, we can treat α as a scalar quantity, instead of a tensor of rank 2.

The AFM cantilever cannot respond at optical frequencies, such as *ω,* so the time-averaged Lorentz force in the dipole approximation is [43]

$$\langle \mathbf{F} \rangle = \frac{\alpha'}{2} \nabla \langle |\mathbf{E}|^2 \rangle + \omega \alpha'' \langle \mathbf{E} \times \mathbf{B} \rangle \tag{2.6}$$

where the particle polarizability is separated by the relation $\alpha(\omega) = \alpha'(\omega) + i\,\alpha''(\omega)$ into α', the real part, and into α'', the imaginary part. We will call the first term the gradient force (also described as the dipole force) and the second term is called the scattering force (or also the absorption force). These two forces will be described separately below.

2.2 Gradient force

The gradient force stems from variations in the electromagnetic field and is proportional to the real (dispersive) part, α', of the complex polarizability. The electric field at the particle dipole is due to both the incident electric field as well as the evanescent field from the induced dipole at the tip, and vice versa. We can model the mutual interaction if we consider the tip and molecule as spheres of volume $\frac{4\pi}{3} r^3$ each with their own effective polarizabilities, as in Fig 2.1, and the induced dipole moments become:

$$\vec{\mu}_{\boldsymbol{t}} = \alpha_t(\mathbf{E}_0 + \mathbf{E}_p) \tag{2.7}$$

$$\vec{\mu}_{\boldsymbol{p}} = \alpha_p(\mathbf{E}_0 + \mathbf{E}_t) \tag{2.8}$$

where $\mathbf{E}_0$ is the electric field of the incident laser, and $\vec{\mu}_{\boldsymbol{t}}$ and $\vec{\mu}_{\boldsymbol{p}}$ are the effective dipole moments of the tip and molecule, respectively. $\mathbf{E}_t$ is the evanescent field of the tip, and $\mathbf{E}_p$ is of the particle. The cantilever response is mostly confined to the z direction and therefore only the z components of the tip and molecule dipoles are relevant, $\vec{\mu}_{\boldsymbol{t}} = \mu_{\boldsymbol{t}}\hat{z}$ and $\vec{\mu}_{\boldsymbol{p}} = \mu_{\boldsymbol{p}}\hat{z}$ respectively. The evanescent fields of the induced dipoles are given as:

$$\mathbf{E}_i = \frac{1}{4\pi\epsilon_0}\frac{(3\vec{\mu}_{\boldsymbol{i}} \cdot \mathbf{r})\mathbf{r} - \vec{\mu}_{\boldsymbol{i}}}{r^3} \tag{2.9}$$

where $\mathbf{E}_i = \mathrm{E}_{ix}\,\hat{\mathrm{x}} + \mathrm{E}_{iy}\,\hat{\mathrm{y}} + \mathrm{E}_{iz}\,\hat{\mathrm{z}}$, $r = \sqrt{x^2 + y^2 + z^2}$, and $i = t, p$ respectively. Using equations (6)-(8) expressions for the z-component of the molecule's induced dipole moment and the electric field at the molecule can be in terms of the tip and particle polarizabilities and incident field in z as:

$$\mu_p = \frac{2z^3\pi a_p\epsilon_0(a_t + 2z^3\pi\epsilon_0)E_{0z}}{4z^6\pi^2\epsilon_0^2 - a_p a_t} \tag{2.10}$$

$$E_{pz} = \frac{a_p(a_t + 2z^3\pi\epsilon_0)E_{0z}}{4z^6\pi^2\epsilon_0^2 - a_p a_t} \tag{2.11}$$

When the relative sizes of the tip and molecule are assumed to be smaller than the gap distance, $z > a_t$ and $z > a_p$, and as the tip and molecule polarizibilities scale with the cube of the radius (Eq. 2.5) we can also safely assume that $z \gg$

$a_p^3 a_t^3$. With these assumptions equations (9) and (10) can be simplified and an expression for the z-component can be described simply as:

$$F_g \equiv \langle \mathbf{F_g} \rangle_z \cong -\frac{3a_p' a_t'}{2\pi z^4} E_{0z}^2 \tag{2.12}$$

There a few significant things to note from equation (11), which is similar to the formula described in [42]. First, the gradient force is attractive. Secondly, there is a z^{-4} spatial dependence, and thus is relevant for only very-short tip-molecule separations. Lastly, the strength of the force is proportional to the dispersive part of the molecule's polarizability and therefore information can be gained about the molecule's optical properties from studying this force. It will be helpful to characterize the magnitude of this force by collapsing the gradient force coefficients into the simple parameter β, as:

$$\beta = \frac{3a_p' a_t'}{2\pi} E_{0z}^2 \tag{2.13}$$

2.3 Scattering Force

The other optically induced contribution, known as the scattering force, predicted by Eq. (2.6) is a repulsive force where the magnitude is proportional to the dissipative part of the light-particle interaction, the imaginary part of the complex polarizability, described as:

$$F_{sc} \equiv \langle \mathbf{F_{sc}} \rangle_z \cong \omega \alpha_t'' \langle \mathbf{E_0} \times \mathbf{B_0} \rangle_z \tag{2.14}$$

where $\mathbf{B_0} = \mathrm{B}_{0x}\,\hat{\mathrm{x}} + \mathrm{B}_{0y}\,\hat{\mathrm{y}} + \mathrm{B}_{0z}\,\hat{\mathrm{z}}$. The transverse components of the electric and magnetic field are the only contributors to the force along the tip axis in the z-direction. The dominant component of the incident field is polarized along x, $\mathbf{E}_0 \approx \mathrm{E}_{0x}\,\hat{\mathrm{x}}$, then the scattering force can be simplified as:

$$\langle \mathbf{F_{sc}} \rangle_z = \frac{2\pi\alpha_t''}{\lambda} E_{0x}^2 \tag{2.15}$$

where λ is the wavelength of the incident beam. Whereas the gradient force scales z^{-4} with tip-sample distance, the scattering force is independent of distance in the nanoscale region of the tip, since the distance-dependence is implicitly contained in the spatial extent of the excitation field E_{0x}. The excitation field dimension in the focal plane is in the (sub)-μm range, the scattering force is manifested over a different spatial scale than the local gradient force. We expect, therefore, that the short range nanoscopic interactions are governed by the gradient force, while at longer distances the scattering force is dominant. The scattering force is generally repulsive unlike the attractive gradient force, so there may tip-sample distance where the two optical forces cancel in magnitude.

2.4 Cantilever Dynamics

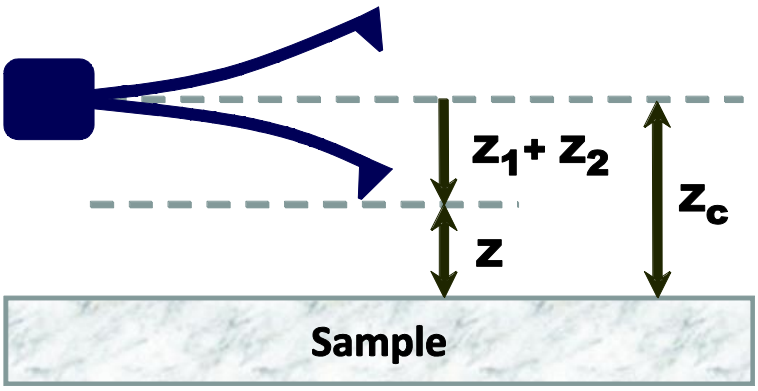

Figure 2.2: Cantilever motion representation, z_1 is the motion of the fundamental resonance, z_2 is of the higher resonance, the instantaneous tip-sample position is given by z and the average position is z_c.

The dynamics of the cantilever-tip system in the presence of the optically induced force, $F_{opt} = F_g + F_{sc}$, can be modeled as a simple harmonic oscillator with motion confined to the z-coordinate only. The relevant motion of the cantilever is between two mechanical resonances of the system for photo-induced force microscopy experiments. The fundamental mechanical resonance of the cantilever is external driven with force F_1 and frequency ω_1, and a higher-order resonance is actively driven by the optical force, F_{opt}. The interaction force, F_{int}, which bundles all relevant van der Waals and Casimir forces present in AFM, acts on the motion of both resonances. In this model, the equations of motion for the displacement of the first (z_1) and higher-order (z_n) mode are found as:

$$m\ddot{z}_1 + b_1\dot{z}_1 + k_1 z_1 = F_1 \cos(\omega_1 t) + F_{int}(z(t)) \qquad (2.16)$$

$$m\ddot{z}_n + b_n\dot{z}_n + k_n z_n = F_{opt}(z(t))\cos(\omega_n t) + F_{int}(z(t)) \quad (2.17)$$

where m is the effective mass of the cantilever; Q_i, k_i, and b_i are, respectively, the quality factor, force constant, and the damping coefficient of the i^{th} eigenmode[44]. For this chapter n=2, which corresponds to the tip motion on the second mechanical resonance but this formalism holds for higher resonances as well. The resonance frequency, driving force, and damping coefficient can be represented by experimental parameters of the AFM system, respectively: $\omega_i = \sqrt{k_i/m},\ F_1 = k_1 A_{01} Q_1$ where A_{01} is the free oscillation amplitude of the driven fundamental mechanical resonance, and $b_i = m_i \omega_i Q_1$. Then the instantaneous tip-surface distance is given by

$$\begin{aligned} z(t) &= z_c + z_1(t) + z_2(t) + O(\varepsilon) \quad (2.18) \\ &\approx z_c + A_1 \sin(\omega_1 t + \theta_1) + A_2 \sin(\omega_2 t + \theta_2) \end{aligned}$$

where z_c is the equilibrium position of the cantilever, A_i is the amplitude and θ_i is the phase shift of the i^{th} eigenmode; $O(\varepsilon)$ is a term that carries the contribution of the other modes and harmonics. Substituting Eq. (2.18) into Eqs. (2.16) and (2.17) by multiplying both sides of the resulting equation by $\sin(\omega_i t + \theta_i)$ and $\cos(\omega_i t + \theta_i)$, followed by an integration over the oscillation period, the following general relations for amplitude, phase, mechanical interaction force and optical force are obtained:

$$(k_1 - m\omega_1^2)\ \frac{A_1}{2} = \frac{F_1}{2}\sin\theta_1\ + \int_0^T F_{int}\ \sin(\omega_1 t + \theta_1)\ dt \quad (2.19)$$

$$\frac{b_1\omega_1 A_1}{2} = \frac{F_1}{2}\cos\theta_1 + \int_0^T F_{int}\ \cos(\omega_1 t + \theta_1)\ dt \tag{2.20}$$

$$(k_2 - m\omega_2^2)\ \frac{A_2}{2} = \int_0^T [F_{int} + \mathrm{F_{opt}}\cos(\omega_2 t)]\sin(\omega_2 t + \theta_2)\ dt \tag{2.21}$$

$$\frac{b_2\omega_2 A_2}{2} = \int_0^T [F_{int} + \mathrm{F_{opt}}\cos(\omega_2 t)]\cos(\omega_2 t + \theta_2)\ dt \tag{2.22}$$

Given a model function for both the interaction forces, F_{int}, and the optical force, F_{opt}, the cantilever dynamics of the oscillation amplitudes of both resonances, A_1 and A_2, and the corresponding phase shifts, θ_1 and θ_2, can be calculated through numerical integration of Eqs (2.19)-(2.22).

2.5 Reconstruction of Interaction Forces

The amplitude and phase of the first and second resonances are experimentally accessible quantities. We next describe an approximate method to relate the forces active at the tip-sample junction to these experimental quantities. In general, F_{int} is a nonlinear function of the tip-sample distance z and contains both conservative and dissipative (i.e., nonconservative) forces,

$$F_{int} = F_c(z) + F_{nc} \tag{2.23}$$

where the conservative term Fc, by definition, depends only on the distance z. For our description here, we assume that the nonconservative force can be

written as $F_{nc} = -\Gamma(z)\dot{z}$, where Γ represents the effective damping coefficient of a given dissipative interaction. Such a form of force may describe many physical interactions such as the van der Waals, electrostatic, hydrodynamic, or capillary meniscus forces[45]. Note that although the term $-\Gamma(z)\dot{z}$ may be replaced by some other specific forms of dissipation, one can still employ the effective and intuitive coefficient Γ as a parameter describing a given dissipation [23, 46].

We use two approximations to simplify the description. First, we assume that the tip displacement is small such that the force at z can be obtained through a Taylor expansion of the force at the equilibrium position z_c. Under these conditions, the mechanical interaction force and the optical force can be expressed by

$$F_{int}(z(t)) = F_c(z) - \Gamma(z)\dot{z}$$

$$\approx F_c(z_c) + \frac{\partial F_c(z)}{\partial z}|_{z_c}(z - z_c) - \Gamma(z_c)\dot{z} \tag{2.24}$$

$$F_{optic}\big(z(t)\big) \approx F_{optic}(z_c) + \frac{\partial F_{optic}}{\partial z}|_{z_c}(z - z_c) \tag{2.25}$$

Second, we assume that the frequency of the first and second mechanical resonance are related as $\omega_2 \approx 6\omega_1$. In practice, the frequency of the 2nd resonance is $6.27\omega_1$ [44]. Although the approximation $\omega_2 \approx 6\omega_1$ gives rise to numerical differences in the integration of Eqs. (2.19)-(2.22), this difference is

small while the general physics of the problem remains preserved. Using the approximation $\omega_2 \approx 6\omega_1$, the forces are simplified to

$$F_c(z) = \int_z^{\infty} [\frac{F_1}{A_1(z)} \sin\theta_1(z) - (k_1 - m\omega_1^2) dz \tag{2.26}$$

$$\Gamma(z) = \frac{F_1}{A_1(z)\omega_1} \cos\theta_1(z) - b_1 \tag{2.27}$$

$$\left|F_{optic}(z)\right| = A_2(z)\sqrt{m^2\left(\omega_2'^2 - \omega_2^2\right)^2 + b_2'^2\omega_2^2} \tag{2.28}$$

$$\omega_2' = \sqrt{(k_2 - \frac{\partial F_c}{\partial z}|_z)/m} \tag{2.29}$$

$$b_2' = b_2 - \Gamma(z) \tag{2.30}$$

The formalism outlined by Eqs. (2.26)-(2.28) makes it possible to reconstruct the distance dependent mechanical and photo-induced force from experimentally accessible parameters.

Chapter Three

Experimental

3.1 Experimental Apparatus

The primary light source for the reported experiments is the Mai Tai HP titanium:sapphire laser, commercially available from Spectra-Physics, with tunable output from 690-1100nm, 80 MHz repetition rate, and a pulsewidth near 150 femtoseconds. The Mai Tai is tuned to a center wavelength of 809nm and the 2.8 W average power pumps an Optical Parametric Oscillator (OPO, Spectra-Physics Inspire AUTO), providing two fs tunable outputs, from 480 nm to 2.5 μm, and also the depleted pump pulse from the Mai Tai. Each pulse train is separately amplitude-modulated by an acousto-optic modulator (AOM, Crystal Technologies) and the dispersion throughout the system is compensated by a folded geometry prism compressor. The beam is also focused through a pinhole spatial filter to clean up the spatial mode; a good Gaussian beam is

useful for aligning the focal spot onto the AFM tip, as described below. The AOM modulation frequency is selected to coincide with the second or third mechanical resonance of the particular cantilever being used in the atomic force microscope. Some of the early gold nanowire images (see 4.2) were taken using a CW-tunable diode laser (Xperay) centered at 702nm.

A commercially available atomic force microscope system (Molecular Vista) was customized over an inverted optical microscope setup with a high NA (1.43) 100x oil-immersion objective (Olympus). The sample is prepared (as below) onto 170μm glass slides fixed to the sample stage scanner where the AFM scan head is mounted. The scan head's low profile and more open geometry allows for transmission optics for sample illumination and alignment as well as simultaneous modular optical detectors in addition to reflection optics and CCD detector. The entire experimental system is vibrationally-isolated on two floating optical tables (Newport and Thorlabs), due to table-space restrictions, weakly-coupled together by mounting plates. The AFM/inverted microscope setup is encased in a home-built acoustic enclosure and otherwise operates under ambient conditions.

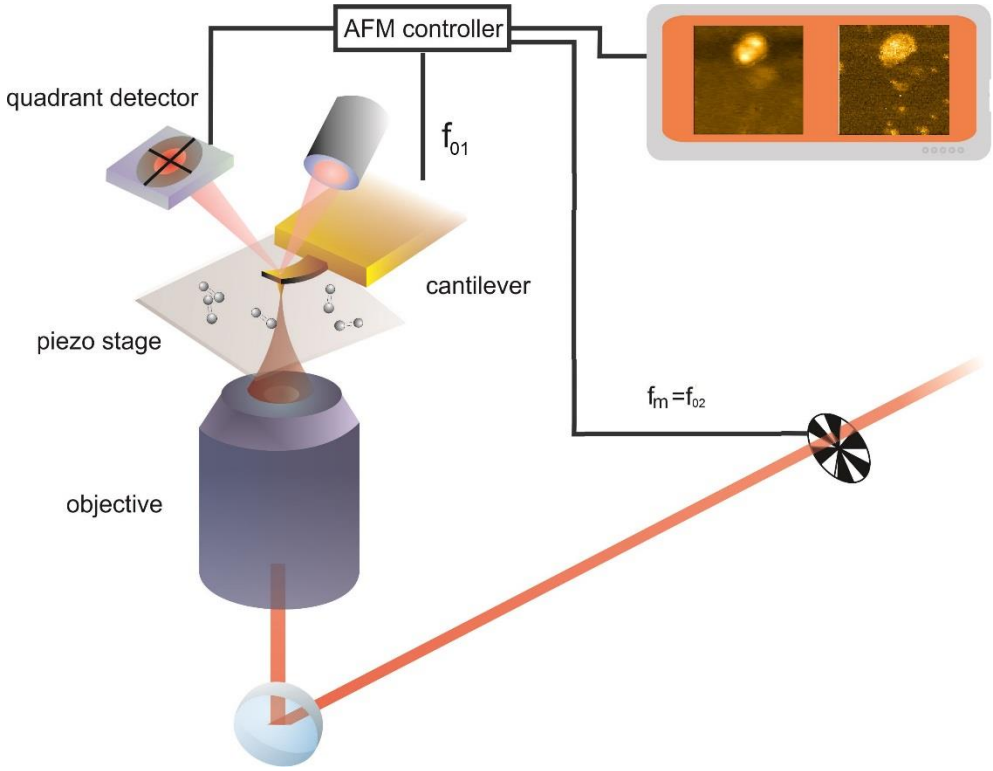

Figure 3.1: Schematic of the Photo-induced Force Microscope system

The Molecular Vista system utilizes a digital function generator with a field programmable gate array which generates synchronized clock signals for the digital lock-in amplifier that allows for multiple channels for signal demodulation. The quadrant detector signal is demodulated at the first and higher-order mechanical resonances. This provides for simultaneous measurements of the sample topography on the first mechanical resonance, f_{01}, and the optical force images on the second (or third), f_{02} (or f_{03}), resonance.

A 10 nm radius commercially gold coated silicon tip is used in the experiments (FORTGG, AppNano). Two cantilever systems are employed. The first cantilever system has k_1 = 1.61 N/m, Q_1 = 181.93, and a first mechanical

resonance f_{01} = 58.73 kHz. The second mechanical resonance of the cantilever is at f_{02} = 372.41 kHz, with k_2 = 52.24 N/m and Q_2 = 561.36. The free oscillation amplitude of the fundamental resonance A_{01} is set to 38 nm in the experiments below. The laser modulation frequency was set to 372.41 kHz for optical force measurements, coinciding with the second mechanical resonance of the cantilever. The second cantilever system exhibits a mechanical resonance at f_{01} = 58.58 kHz with k_1= 1.6 N/m and Q_1 = 178, operated with a free oscillation amplitude A_{01} = 32 nm. The optical force measurements with this system are carried out at the third mechanical resonance of the cantilever, which is found at f_{03} = 1033.190 kHz. The corresponding spring constant and quality factor of this resonance are k3 = 492.51 N/m and Q_3 = 539, respectively.

Before the microscope the linear polarization is controlled by a half-wave plate (denoted as x-polarization). The high NA microscope objective tightly focuses to a diffraction-limited spot, which generates significant electric field components in the y-direction as well as in the longitudinal z-axis, the field intensity profile is given in Figure 3.2.

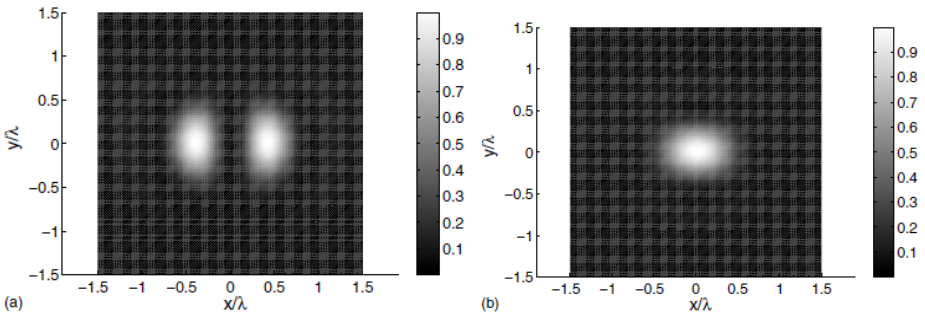

Figure 3.2: (a), Longitudinal field intensity $|E_z|^2$ and (b) total intensity $|E|^2$in the focal region of the X-Y plane [47]

The positioning of the tip within the focal spot is critical to the alignment. With the sample stage and optical focus fixed, the AFM head is scanned over the focal spot and on the higher-order mechanical resonance an image of the light-tip interaction is produced. The tip is most sensitive to the force components along its axis in the z-direction, and under the proper conditions the two lobes of the longitudinal field intensity can be seen, as in Figure 3.3. However, the scattering force is strongest at the center of the focal spot, which may contribute to the distortions from the expected two-spot image. The tip is positioned at the peak of the light-tip interaction and the sample stage is then scanned with the tip and focal spot held fixed.

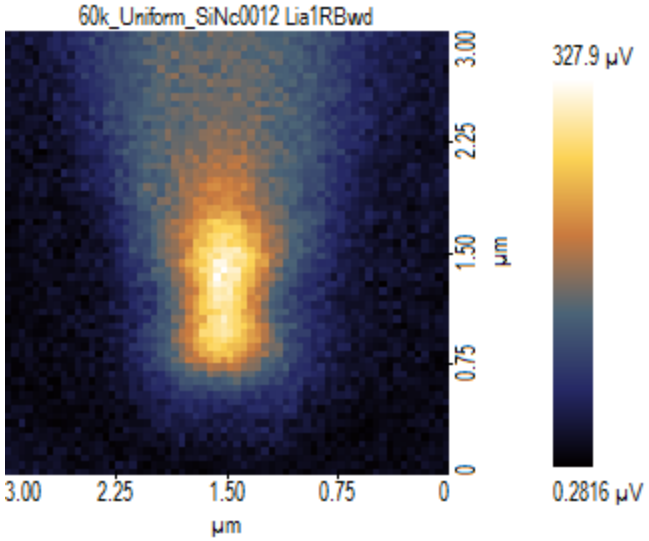

Figure 3.3: AFM head scanned over the focal spot, mapping the optical force interaction of a SiNc thin film

3.2 Sample Preparation

Studies were conducted on two samples of interest. Silicon naphtalocyanine (SiNc) was commercially available from Sigma-Aldrich (389935). SiNc was dissolved in Toluene and then spin-coated onto plasma-cleaned standard 170 µm microscope slides. After the toluene evaporates the SiNc forms nanoscale clusters of varying dimensions, down to less than 10 nm. An absorption spectrum was taken with a Cary 50 spectrophotometer of one of the SiNc sample slides. The excitation pulse is tuned to overlap with a significant portion of the SiNc absorption peak, but not centered over it due to the OPO's pump power requirements. SiNc was chosen as a model chemical for its high

absorption cross-section (Figure 3.4), as well as an exceptionally high cross section for excited state absorption useful for future nonlinear optical experiments [48].

The other samples considered were gold nanowires. The nanowires are fabricated onto the same standard microscope slides by the lithographically patterned nanowire electrodeposition technique carried out by the Penner group[49].

The nanowires feature an average width of 120 nm and an average height of 10-25 nm, with the length of the nanowires extending over millimeters. The average power of the laser beam at the sample plane is between 23 μW and 38 μW, depending on the experiment.

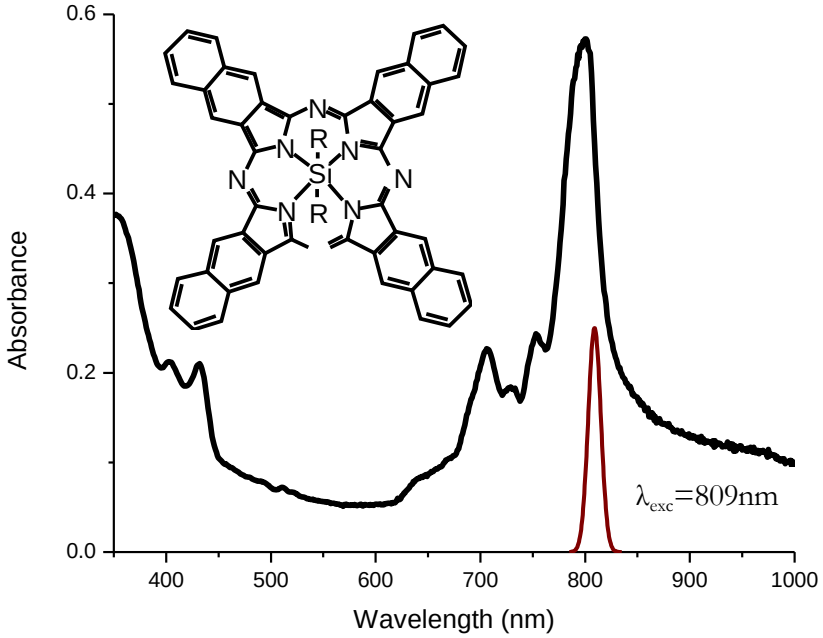

Figure 3.4: Chemical structure and linear absorption spectrum of SiNc and the excitation pulse shape in red

Chapter Four

Results and Discussion

4.1 Force-distance simulations

From the expressions derived for the cantilever dynamics of the amplitude and phase of both resonances simulations can be run of the general dynamics once a functional form is chosen for the electrostatic/mechanical forces, F_{int}, and the optically induced interactions, F_{opt}. Assuming F_{int} can be described as a conservative Lennard-Jones model with $1/z^6$ (repulsive) and a $1/z^2$ (attractive) force terms of the form,

$$F_{int} = f_0 \left(\frac{l^4}{3z^6} - \frac{1}{z^2} \right) \tag{4.1}$$

where f_0 is a constant and l is the characteristic distance at which the attractive force is minimized. The photo-induced forces are modeled by both the gradient force and the scattering force from Eqs. (2.12) and (2.15),

$$F_{opt} = -\frac{3\alpha_t'\alpha_p'}{2\pi z^4} E_{0z}^2 + \frac{2\pi\alpha_t''}{\lambda} E_{0x}^2 \tag{4.2}$$

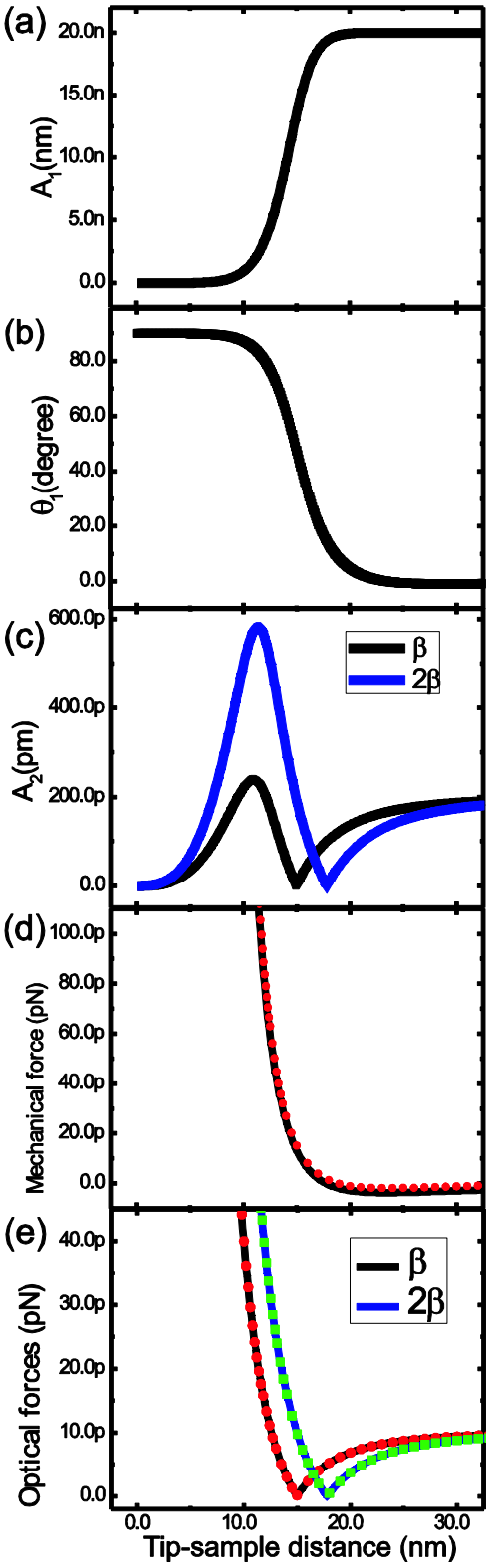

Figure 4.1: Simulation of the amplitude (a) and phase (b) of the first resonance as a function of tip-sample distance, with a free oscillation amplitude of 20nm. (c) Comparison of second resonance amplitude-distance curves for F_g system with β and 2β. (d) Lennard-Jones type force (black) and reconstructed force (red dots). (e) F_g comparison with β and 2β and reconstructed force (dots). Simulation parameters based on typical experimental values are: f_0=3× 10^{-27} N·m^2, : $f_0 l^4/3$=3× 10^{-55} N·m^6, F_1= 16× 10^{-11} N, β = 5 × 10^{-43} N·m^4, k_1=1.6 N/m, k_2=62.9 N/m, ω_{01}=60 kHz, ω_{02}=376.2 kHz, Q_1=200, Q_2=1254, F_{sc}=1× 10^{-11} N.

Figure 4.1 shows that the first resonance amplitude (a) and phase (b) curve follows the expected trend for a cantilever interacting with Lennard-Jones type forces. On the higher-order resonance the amplitude curve (c) is quite different due to the presence of F_{opt}. At further distances there is a plateau that is due to the repulsive scattering-force, independent of β and tip-sample spacing. At shorter distances the attractive F_g dominates and a peak is observed that is dependent on the effective polarizability magnitude. The dip is the point where the scattering and gradient optical forces cancel. When the gradient force parameter β is doubled the peak second resonance amplitude is correspondingly increased, but also the dip where F_g and F_{sc} cancel is shifted to further distances, while the F_{sc} plateau is unchanged.

Now having used an assumed functional form for F_{int} and F_{opt}, we can reverse this and use Eqs. (2.26)-(2.28) to reconstruct the optical and mechanical forces from the simulated amplitude-distance curves. This is done for the simulated amplitude-distance curves, (d) and (e), to demonstrate that the assumptions used in the theoretical description are valid, and that the form of the optical force can be extracted from experimental amplitude-distance curves. Again, we see in (e) that differences in β shift the F_g and F_{sc} cancellation point and subsequently image contrast can vary dramatically. Depending on the cantilever set-point the contrast between a sample with a high F_g and substrate can be positive, negative, or nonexistent, which demonstrates that knowledge of the force-distance curve is necessary for microscopy interpretation.

4.2 Photo-induced forces near gold nanowires

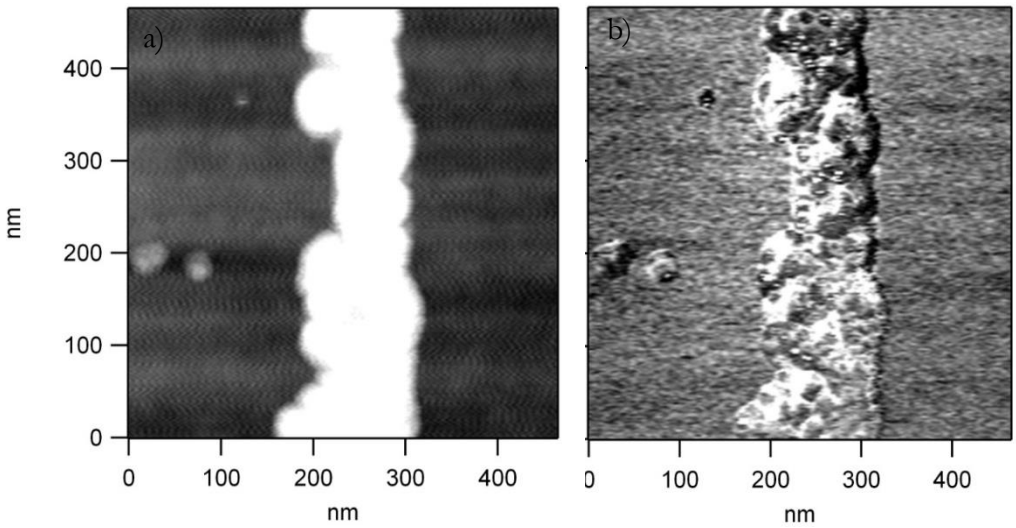

Figure 4.2: AFM topographical image (a) of a gold nanowire, and optical force image (b) illuminated with a 702nm CW-laser

Gold nanowires deposited on a glass surface were chosen as a test material. Figure 4.2 shows much higher structural contrast on the optical force image, under cw-illumination, than the standard topography, and while it may not necessarily be optimized for topography this demonstrates the use of this technique for imaging contrast. The force cross sections between thick gold clusters and the thinner sections in Figure 4.3 show the short-range nature of the gradient force contrast and subsequent insensitivity to bulk properties.

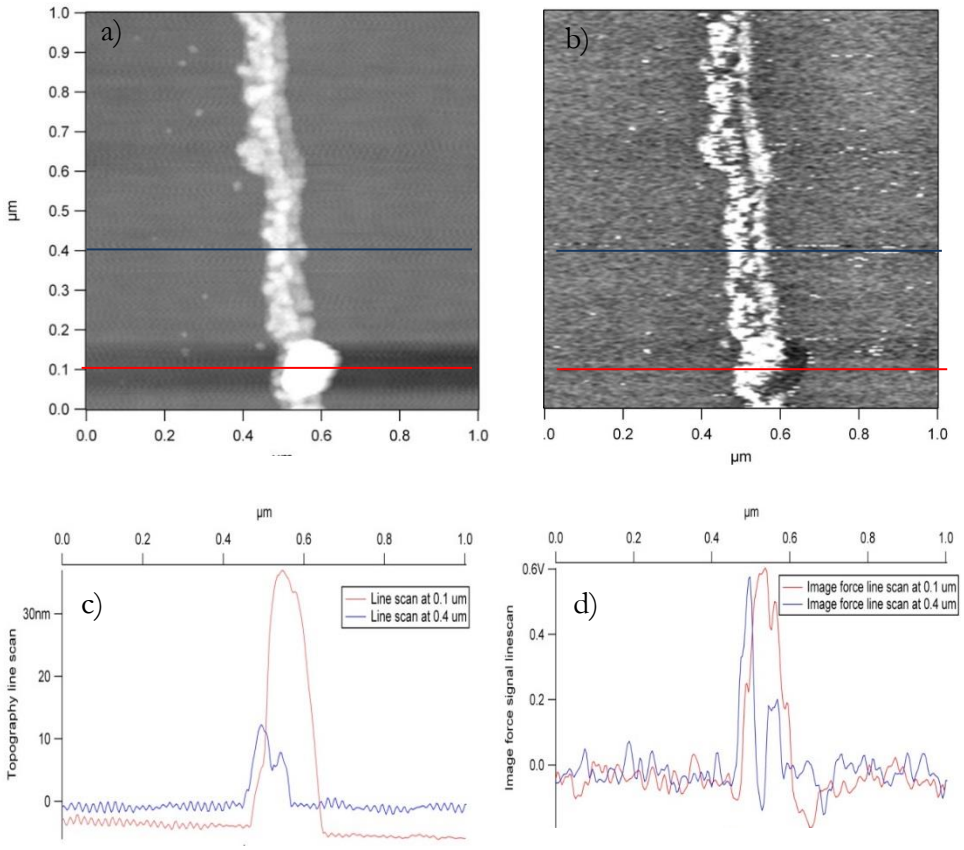

Figure 4.3: Gold nanowire topography (a) and optical force image (b), the corresponding linecuts, (c) and (d) respectively, show the very local nature of the gradient force

However, interpretation of the contrast in Figure 4.2 is difficult as it requires knowledge about the exact spatial form of the optical forces of Figure 4.3. A first step towards a more complete interpretation of the image contrast is the reconstruction of the optical force from the experimental amplitude-distance curves by using the formalism developed in Chapter 2. In Figure 4.4, amplitude-distance curves are shown for a single location on a gold nanowire under fs-

illumination. In Fgure 4.4c the characteristic peak and a small dip can be seen in the second resonance amplitude, before the tip reaches the contact-mode regime, noted in blue, and settles to a value ~75pN. In that region the thermal expansion of the nanowire dominates, and A_1 and θ_1 do not vary. Further away the sample and the scattering force gives rise to the plateau seen in A_2.

The optical force is reconstructed in Figure 4.4d and fitted in red by Eq (4.2) to estimate the strength of the scattering force interaction and the gradient force pre-factor, as F_{sc} = 6:13 pN and $\beta = 2.26 \times 10^{-40}$ N·m^4 respectively. The contact mode regime at short distances appears as a plateau before the gradient force interaction dominates before dip where $F_g + F_{sc} = 0$ and it begins to level off to the scattering force value mentioned above. However at the dip the force does not reach zero due to thermal noise at the second resonance frequency, which shows as an offset[50, 51].

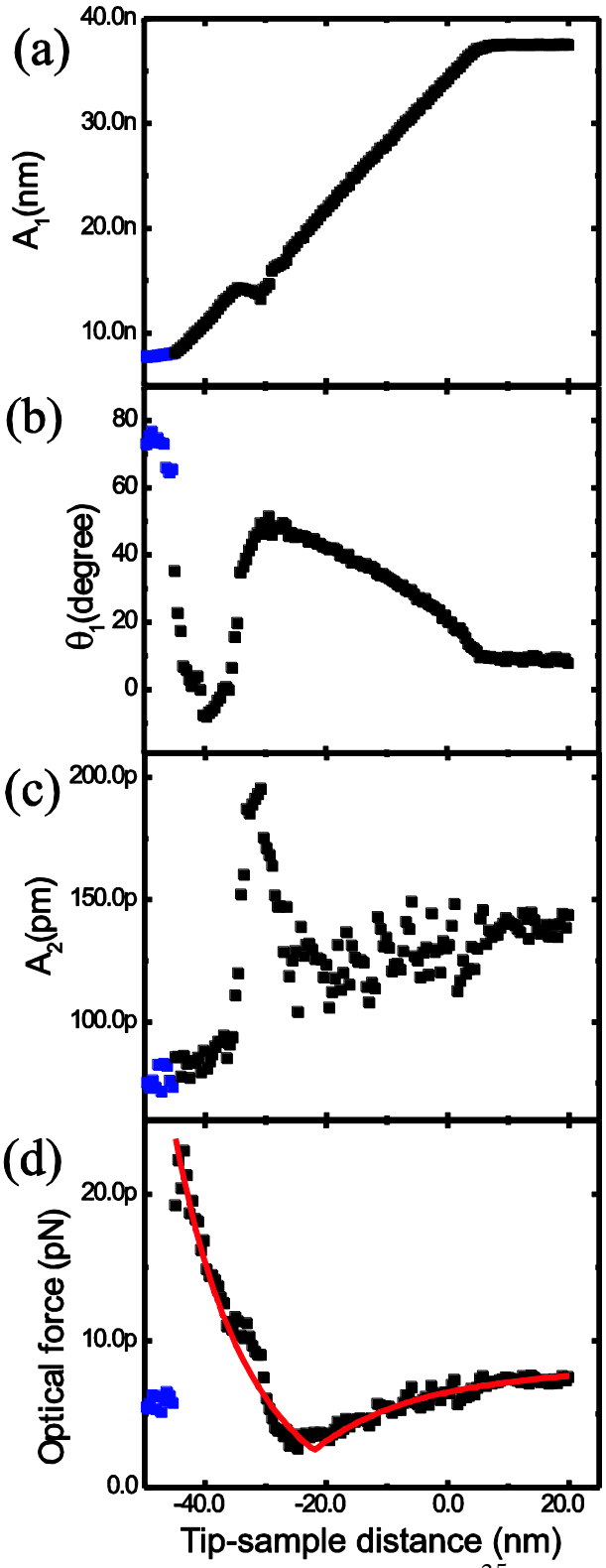

Figure 4.4: The amplitude (a) and phase (b) of the first mechanical resonance on a gold nanowire, the second resonance is driven under 809nm fs-illumination and A_2 with respect to tip-sample distance is given in (c). The optical forces (d) are then reconstructed from the amplitude and phase curves.

4.3 Photo-induced forces and molecular resonances

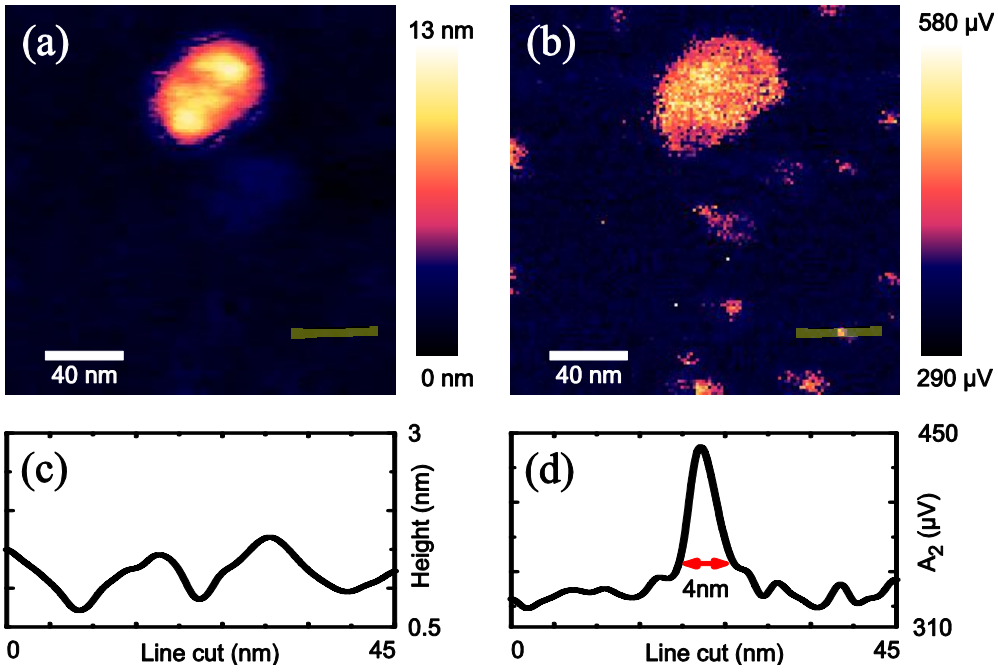

Figure 4.5: Silicon naphtalocyanine (SiNc) nanoclusters imaged in topography (a) and simultaneous photo-induced force imaging (b) in resonance with the absorption band, corresponding line-cuts shown in green for topography (c) and in the optical force case (d) resolve smaller clusters more clearly.

The next test material studied with photo-induced force microscopy is silicon naphtalocyanine (SiNc), chosen for its high absorption cross section (Fig. 3.4) that is roughly resonant with the 809nm fs pulse. In Figure 4.5, simultaneous topographical and optical force images are shown of SiNc nanoclusters. Many of the smaller features are detectable only in the optical force images, with sizes

down to the approximate spatial resolution of the AFM tip. In a previous optical force experiment, this has been seen and attributed to very small copy numbers of similar dye molecules[40]. In the larger cluster of SiNc molecules, topographical variation is seen that is not as evident in the optical force image, which is due to the effect's extremely local nature and its insensitivity to volume effects.

Force-distance measurements were taken over a SiNc nanocluster and are shown in Figure 4.6. In contrast to the force-distance measurements on the gold nanowires, the laser modulation frequency was chosen to overlap with the third mechanical resonance, at f_{03} =1033.190 kHz, of the cantilever. This higher frequency reduces the thermal noise contributions. The optical force-distance curve is extracted in the same way from the amplitude and phase data, and in Fig. 4.6d we see that that the point where $F_g + F_{sc} = 0$ is on a lower offset due to the higher modulation frequency. Again, from fitting the reconstructed optical force data to Eq. 4.2), shown in red, we can extract the force parameters, found to be F_{sc} = 59:0 pN and $\beta = 6.10 \times 10^{-43}$ N·m^4.

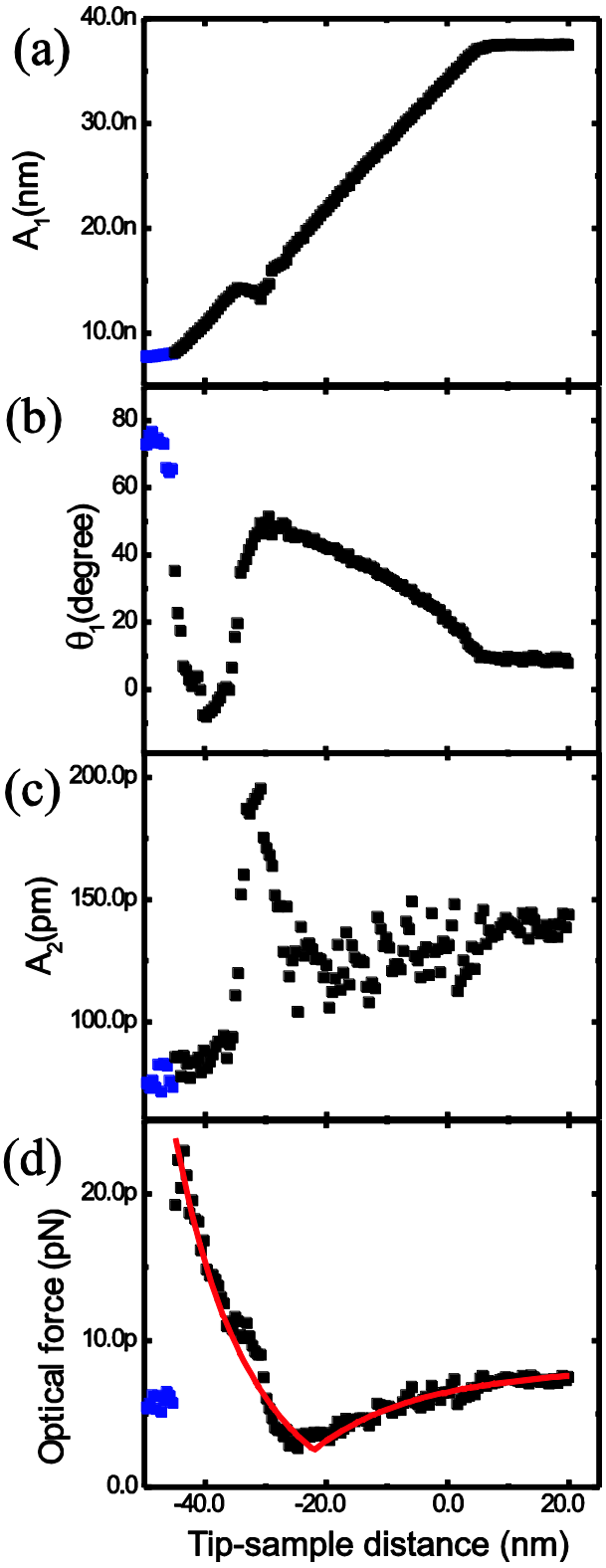

Figure 4.6: Force-distance curves for the amplitude (a) and phase (b) of the first mechanical resonance over a nanocluster of SiNc, and third mechanical resonance amplitude (c) driven in resonance with 809nm fs-pulses. Reconstructed optical force (d) with fit in red.

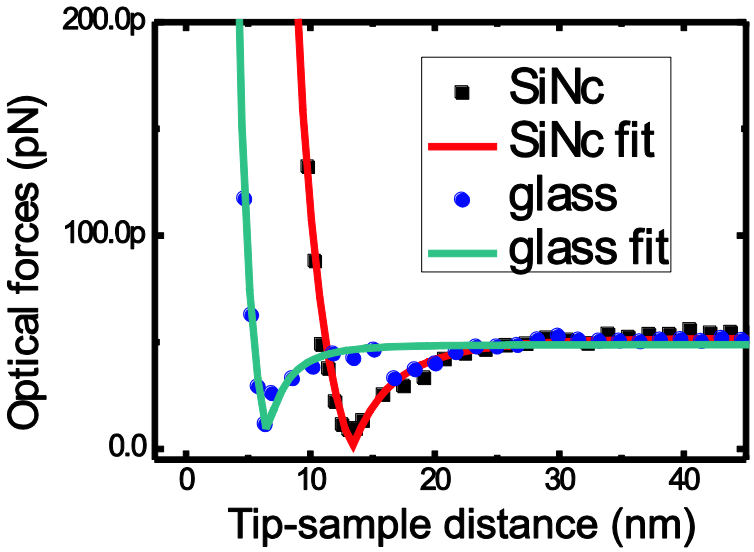

Figure 4.7: Comparison of reconstructed optical force data and corresponding fits for SiNc and glass slide substrate.

On another cluster of SiNc force-distance measurements were taken then the tip was moved onto the glass substrate nearby and the force spectroscopy was re-run for comparison. The reconstructed optical forces and corresponding fits are shown in Figure 4.7. The extracted scattering force, F_{sc} = 52.1 pN for the SiNc cluster and F_{sc} = 45.3 pN for the glass surface, is relatively similar for both materials, which is expected from the optical force equation (4.2) as the scattering force contribution is independent of sample polaribizilities and is governed by the optical response of the tip. For the gradient force coefficient we found for the SiNc cluster $\beta = 1.64 \times 10^{-42}$ N·m^4 and for the glass surface $\beta = 1.75 \times 10^{-43}$ N·m^4. Due to the optical resonance with the 809nm pulse the gradient force is strongest in SiNc and subsequently the $F_g + F_{sc} = 0$ point is shifted to further

sample distances. This was theoretically shown in Fig. 4.1e and highlights the need for an understanding of the set-point to gain good imaging contrast. This also shows that that the gradient force is a sensitive probe of material optical properties on the nanoscale.

Chapter Five

Pump-Probe Force Microscopy

5.1 Introduction

Pump-probe microscopy enables the investigation of ultrafast dynamics in matter on the characteristic time scales of its electronic and vibrational excitations. Pump-probe optical microscopy techniques provide fluorescence-free and label-free imaging contrast [52], but generally rely on large ensembles to produce strong optical signals where the unique response from individual particles is lost and the spatial resolution is diffraction-limited, which obscures differentiation in heterogeneous samples on the nanoscale.

Optical pump-probe in the far-field towards single molecule sensitivity [53] remains very difficult because optical detection of the pump-probe effect relies on measuring a pump-induced intensity change in the scattered probe and therefore is not background free. While using optical excitation combined with

scanning-probe techniques can reduce the spatial limit beyond the diffraction limit and near-field pump-probe techniques have utilized fs infrared pump-probe to change the local plasmonic SNOM-tip excitation to investigate plasmon dynamics in graphene [54], study the nonlinear response of quantum dots using pump-probe induced transient reflectivity [55], and to study exciton dynamics with SNOM-collection of the probe [56]. However, these still rely on the optical detection of the probe variation which is not background free and presents difficulties to reach the single molecule limit.

Non-optical detection then offers a promising alternative towards improving the detection sensitivity towards the single molecule limit with nanoscale spatial resolution. The photo-induced microscope is capable of probing various forms of optical interaction, including nonlinear processes, as demonstrated for stimulated Raman scattering under CW illumination [42], through the non-contact mechanical detection of optical transitions by measuring the gradient force between the light-induced dipoles in the tip and molecule. We have shown the feasibility of using fs pulses in PiFM experiments and can now apply the technique to ultrafast pump-probe processes at the nanoscale, without the problems associated with the presence of a large optical background. Here we will investigate the excited state dynamics of SiNc and then demonstrate that the PiFM is sensitive to the same temporal dynamics as conventional optical pump-probe microscopy.

5.2 Pump-probe Basics and Nonlinear Optical Spectroscopy

In order to understand and prepare for the nonlinear photo-induced force microscopy experiment of SiNc the optical response, thermal properties, and relevant timescales has to be well understood. This was accomplished through optical pump-probe microscopy, where the detection mode is optical rather than force detection. The optical pump-probe experiment was carried out to determine the excited-state lifetimes and microscopic structure of deposited SiNc. Here, two ultrafast pulses are used, where the pump pulse sets up the system of interest by exciting it, and after a controlled time delay, the probe pulse subsequently investigates the transient states created. Various contrast mechanisms can be employed in pump-probe microscopy depending on the pulse timing and molecular wavelength response, which includes stimulated emission, ground state depletion, and excited-state absorption, illustrated in fig. 5.1.

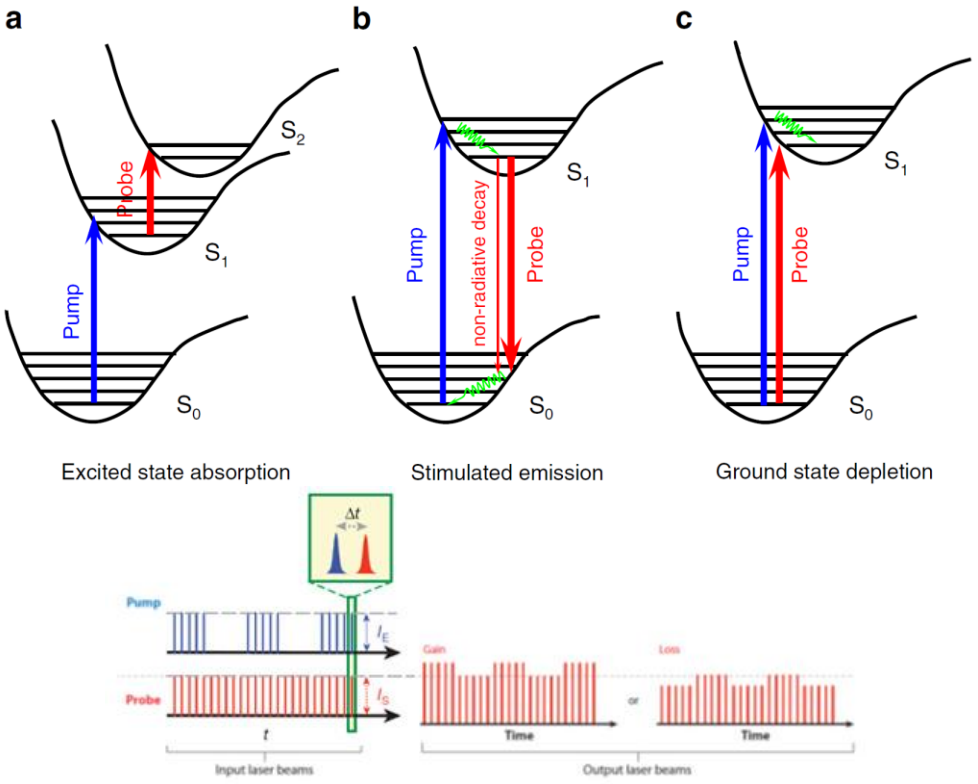

Figure 5.1: Pump-probe microscopy energy-level diagrams of a) excited state absorption, b) stimulated emission, and c) ground state depletion, d) typical energy transfer modulation scheme. [57, 58]

The detection of these processes in microscopy relies on a modulation transfer scheme, where the pump pulse train intensity is modulated at high frequency by an acousto-optical modulator (AOM) and the probe pulse train picks up this modulation through interaction with the sample and is detected by a lock-in amplifier, where the probe pulse experiences a relative gain or loss in amplitude depending on the interaction.

In stimulated emission microscopy the pump pulse sets up an excited electronic state in the molecule, which is stimulated back down to its ground state by the

probe pulse when the frequency is matched to this transition and a new photon coherent to the probe is emitted with the same phase, frequency and polarization. With the addition of these new photons the demodulated probe pulse experiences an increase in the in-phase signal. This signal can be maximized by introducing a time delay to allow for fast vibrational relaxation in the excited state, enabling efficient stimulated emission from the lowest lying singlet excited state.

Ground state depletion microscopy has been used for absorption imaging contrast down the single molecule level [53]. When both the pump and probe pulses are resonant with the absorption of the molecule, the absorption of the pump pulse causes the probe pulse to be absorbed less, resulting in a relative gain in the in-phase probe detection channel. When the pump is absent the probe is attenuated through absorption from the ground state.

In excited state absorption microscopy the pump excites the molecule to an excited electronic state and afterward the probe can further excite the system to a higher state. When the pump is not present the probe is not absorbed (or to a lesser extent) and there is a gain in the transmitted probe pulse train which corresponds to an 180° phase shift to the pump modulation. The demodulated signal is maximized by a few hundred femtosecond delay to allow vibrational relaxation in the excited electronic state. The lifetime of the excited state S_1 can be characterized by controlling the delay between pulses.

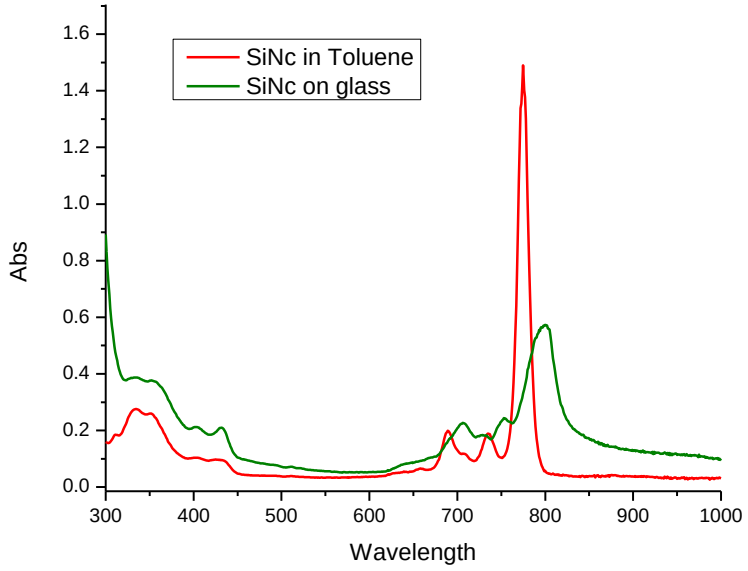

Figure 5.2: Linear absorption spectrum of SiNc in toluene solution and dried on glass substrate

Linear and time-resolved nonlinear absorption experiments were carried out on SiNc in solution to gain insight into the transient absorption spectrum. Naphthalocynanines possess significant nonlinear susceptibilities, high chemical and thermal stability, and their excited state absorption has been theoretically considered [48].

Here, a Ti:sapphire chirped pulse amplified system (CPA-2001, from Clark-MXR Inc.) was used as the light source for a transient absorption experiment of SiNc dissolved in toluene. The linear absorption spectrum shown in Fig. 5.2 shows that the SiNc dried on a glass slide is red-shifted from the solution, due to the

strength of the interaction between the dye and the substrate. The 150 fs laser output was tuned to 775nm accordingly, and split in two parts, one used as the pump pulse, and the other path passed through a 1 cm water cuvette to generate white light continuum and used as the probe pulse. The two pulses were focused into the SiNc solution cuvette and the probe beam was spectrally resolved with a monochromator (150mm Acton Spectra Pro 150), while a mechanical delay line introduced temporal separation. Figure 5.3 shows the change in transmission of the spectrally-broad probe beam across roughly 70 ps of pump-probe delay. The peak in excited state absorption is seen at a probe wavelength of 605 nm, and at approximately ~700 nm the transient absorption reverses sign to positive and ground state depletion dominates the response as the probe pulse begins to overlap with the absorption spectrum. At the excited state absorption peak the decay of the primary relaxation pathway from S_1, with lifetime τ_1, was found to be approximately 7.9 ps.

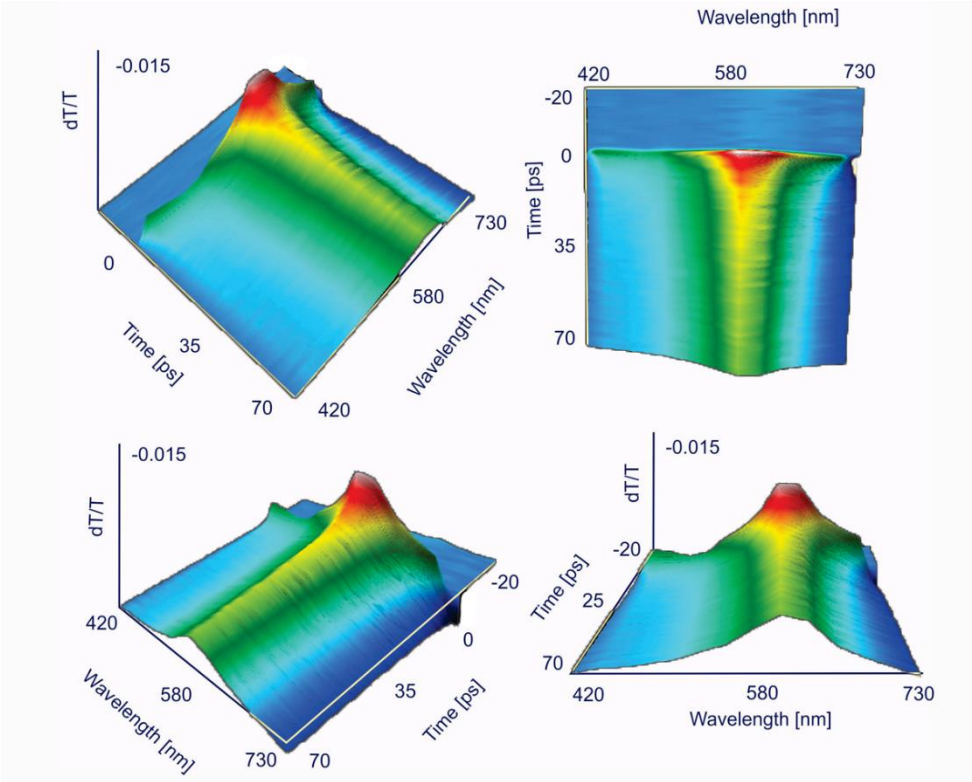

Figure 5.3: Excited state absorption spectrum with broad probe and time delay, in 3D representation from several perspectives

5.3 Pump-probe Optical Microscopy of SiNc

To directly compare pump-probe microscopy results taken optically at the diffraction limit with pump-probe force microscopy at the nanoscale, an all-optical experiment was conducted with similarly prepared samples. The optical pump-probe microscopy experimental setup (illustrated in Figure 5.4) uses the ultrafast light source and OPO described in Section 3.1 and employs both

outputs, the probe pulse from the OPO signal output and the pump pulse from the depleted Mai Tai laser. The two pulses are temporally overlapped with a motorized stage providing adjustable delay and then spatially combined on a dichroic mirror. The pump pulse is intensity modulated by an acousto-optical modulator at 5MHz whereas the probe is not modulated. The high modulation frequency is needed to overcome laser intensity noise at lower frequencies, known as $1/f$ noise.

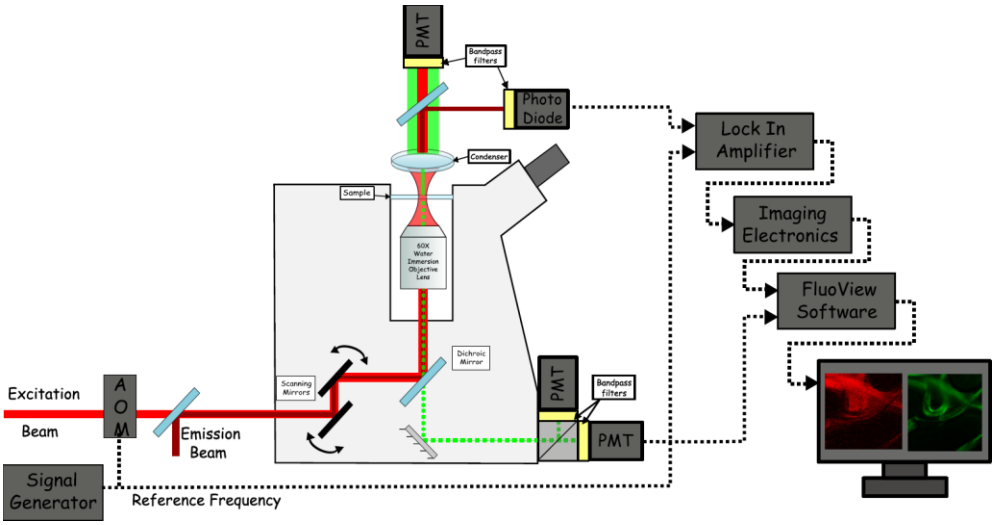

Figure 5.4: Schematic of optical pump-probe microscopy system[59]

The overlapped pulses enter the scanning microscope (commercial Olympus IX-81 and Fluoview scanning unit) where the focal spot is scanned over the sample plane through a NA 1.43 (oil), 100x objective lens. After the interaction with the sample, the transmitted probe is separated from the pump, which is detected for

transmission imaging, using a dichroic mirror and a bandpass filter before being detected by a fast photodiode. In the epi-direction, scattered photons are spectrally filtered to isolate the electronic CARS anti-Stokes emission and detected by a photo-multiplier tube (PMT) to simultaneously measure the electronic CARS signal for understanding the image contrast and temporally synchronizing the pulses.

The photodiode signal is filtered with an electrical bandpass filter and directed to a lock-in amplifier (HF2 Zurich), which is synchronized to the AOM modulation frequency. The lock-in amplifier measures the modulation transfer to the probe from the pump through the contrast-interactions with the sample described above. This signal is scaled appropriately for contrast and input into the microscope software for synchronized pump-probe, CARS, and transmission imaging.

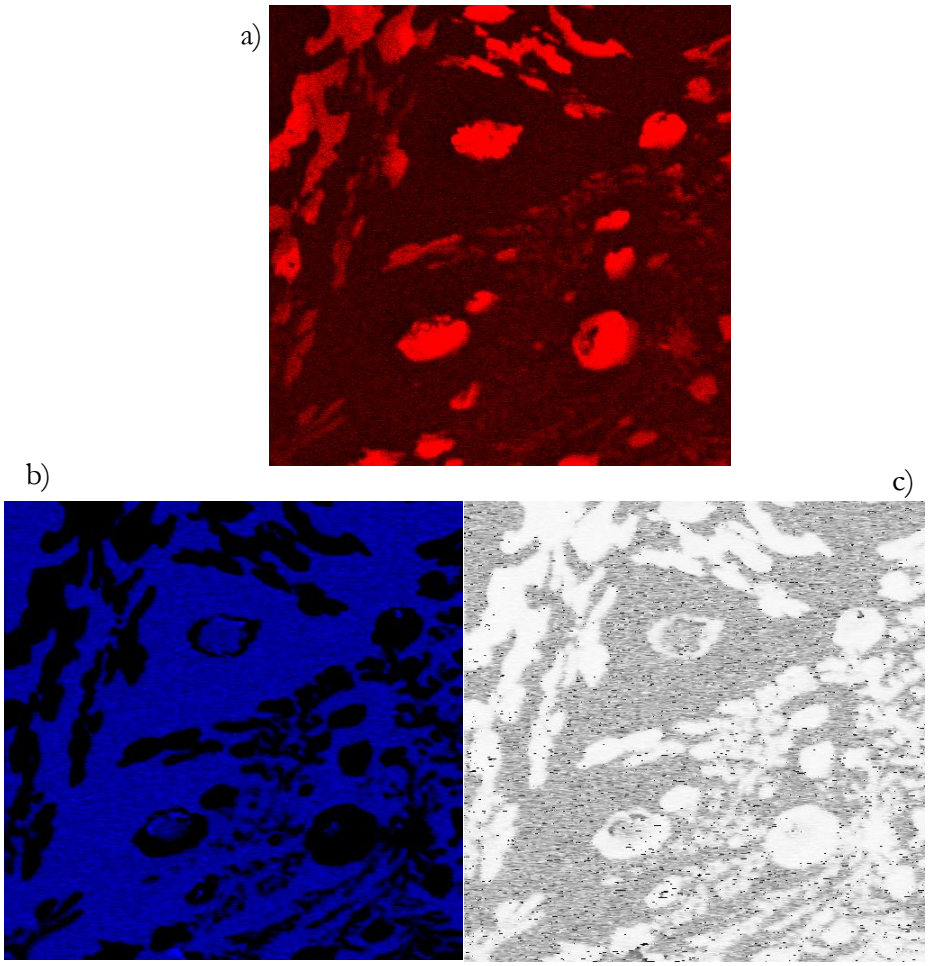

Figure 5.5: Nonlinear optical imaging of SiNc clusters with a) electronic CARS, b) magnitude of transient absorption and c) phase of and transient absorption, image size is 32μm x 32μm.

Again, the SiNc was spin-coated onto microscope slides forming nano and μ-scale clusters of varying morphologies, down to less than 10 nm determined by AFM. In the images shown in figure 5.5, the pump pulse was tuned to 809nm, near the peak of the linear absorption and intensity modulated at 5MHz, the probe pulse was tuned to 719nm and was detected by the forward photodiode, both pulses were approximately 40μW average power at the sample. The back-

scattered light was optically filtered at the CARS emission centered at 647nm and the subsequent PMT signal provides the CARS four-wave mixing image shown in (5.5a). The image shows the aggregation of SiNc into small clusters. The demodulated x-component of the pump-probe signal is shown in (5.5b) and the phase information in (5.5c), the contrast of the SiNc clusters is negative in regards to the glass substrate background and the phase is shown to be shifted by 180° and is indicative of an excited state absorption process. Excited state absorption is expected at this probe wavelength.

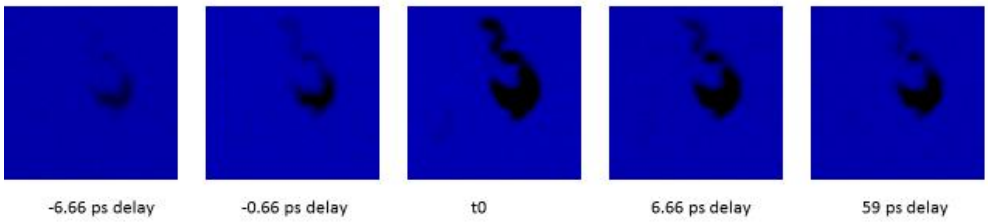

Figure 5.6 Excited state absorption of a SiNc cluster at various pulse delays, resolution is diffraction-limited and the image size is 6.5 μm x 6.5 μm

To determine the temporal dynamics of the excited state absorption of SiNc, a time delay is introduced through a mechanical stage in the probe beam path, where the microscope takes an image at each time setting. The probe beam was tuned to the absorption peak, 605nm, of the excited state, and the pump, 809nm, remained tuned near the linear absorption peak; the average powers at the sample were 180 μW and 58 μW respectively. In Fig 5.6 the pump-probe image of a SiNc cluster is shown for various pulse delays, and some residual contrast is seen

at negative delay timing, which may indicate the presence of a relaxation pathway that is longer than the time between successive pump pulses, at least over 12.5 ns.

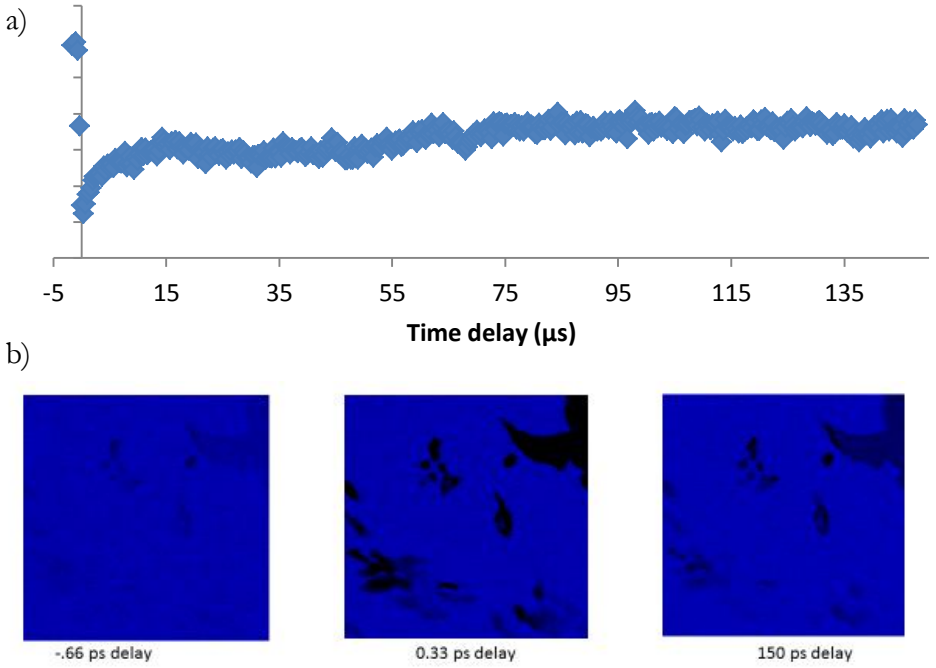

Figure 5.7: Excited state absorption decay dynamics of SiNc cluster for 809nm pump excitation and 605nm probe absorption, a) demodulated in-phase signal with arbitrary y-axis units and b) microscopy images at different time delays, size is 32µm x 32µm

Figure 5.7 shows the excited state decay curve for a microscopic cluster of SiNc over the entire range of the mechanical delay stage. Temporal overlap and t0 is determined by the maximum CARS signal, which is only present when the pulses are overlapped. Figure 5.8 shows the decay of the primary relaxation pathway from S_1, with lifetime τ_1, was found to be approximately 8 ps, in agreement with the optical spectroscopy results.

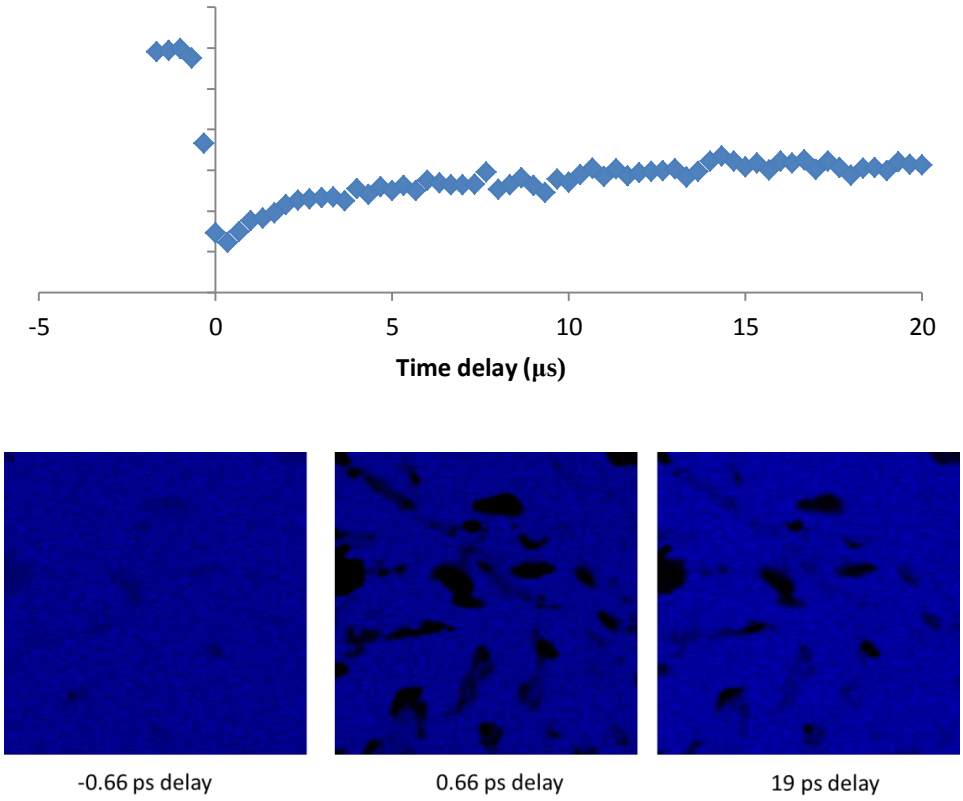

Figure 5.8: Decay dynamics showing rise times and excited state absorption peak, and 25 μm x 25 μm images.

5.4 Nonlinear Ultrafast Photo-induced Force Microscopy

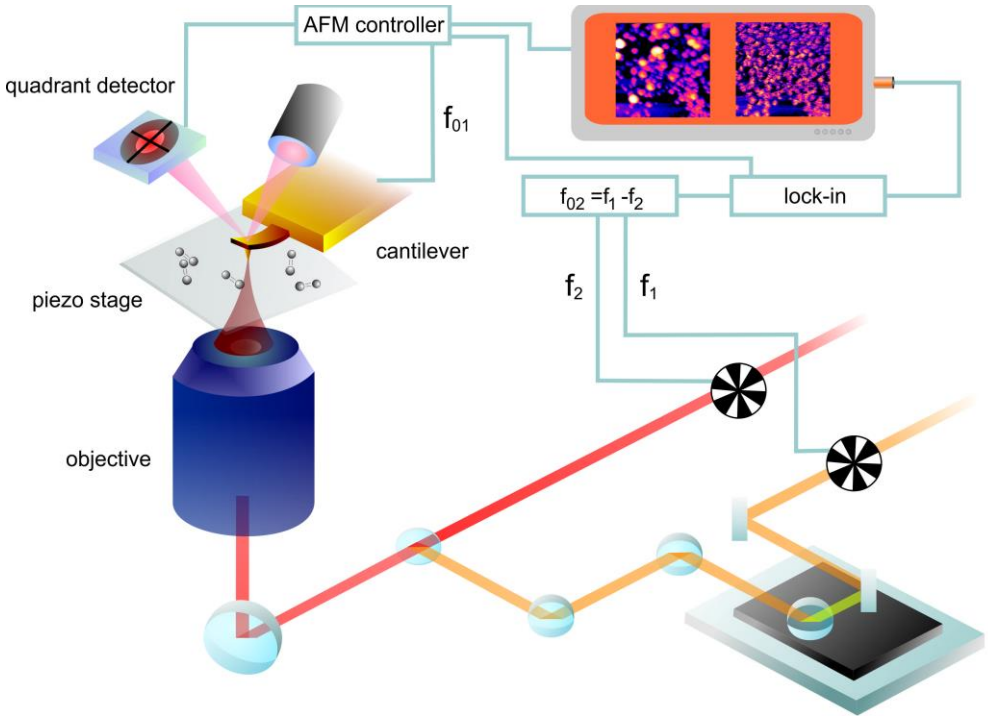

Figure 5.9 Photo-induced force microscope for nonlinear processes

The nonlinear optical microscopies described above that provide rich spectrally-resolved information on the ultrafast time-dynamics of chemical systems are limited in terms of spatial resolution and ensemble effects. However, the photo-induced force microscopy discussed in previous chapters can be extended from the previous linear absorption and CW Raman work into the ultrafast regime of pump probe microscopy on the nanoscale [42]. This allows spatial resolution

beyond the diffraction limit, on the order of ten nanometers, and does not rely on the monitoring the change in intensity on top of the probe background.

The pump-probe extension of the optical force microscope, shown in Fig. 5.9, is comprised of the addition of another pulse train from the OPO, its amplitude is modulated at a separate frequency and the temporal delay is controlled with a mechanical stage. The experiments were carried out between two microscope systems, the Molecular Vista commercial system described in Section 3.1, or with the Olympus IX-81 microscope base modified with a scanning sample stage and a Nanosurf FlexAFM.

The pump, at optical frequency ω_1, and the probe, at ω_2, are amplitude modulated by separately driven AOMs at frequencies f_1 and f_2 respectively. The pump and probe pulses together prepare induced dipoles in the tip-molecule junction and the field gradient between the tip and the molecule results in a gradient force. For a nonlinearly induced polarization that is third-order in the fields, $P^{(3)}$, the time-averaged force is described as[16]:

$$\langle \mathbf{F} \rangle \propto \mathrm{Re} \int d\mathbf{r}\, P^{(3)}(\mathbf{r}) \cdot \nabla \mathbf{E}_2^*(\mathbf{r}, \omega) \tag{5.1}$$

where $\mathbf{E_2}$ is the total probe field in the junction, and $\mathbf{r}$ is the molecule's position relative to the tip dipole. For comparison, in the optically-detected case the signal S, detected at the far field position $\mathbf{R}$ is seen as [60]:

$$S \propto \mathrm{Im} \int d\mathbf{r}\, P^{(3)}(\mathbf{r}) \cdot \mathbf{E}_2^*(\mathbf{R}) \tag{5.2}$$

Here we see that while both methods are based on the coherent mixing of the complex nonlinear polarization with the probe field, the force in PiFM depends on the real part of the interaction and the polarization mixing occurs with the field gradient in the near-field, whereas the optical signal comes from the imaginary part and the mixing occurs at the far-field detector.

The amplitude modulation frequencies of the pump and probe are chosen so that the difference directly overlaps with the second mechanical resonance of the AFM cantilever, $f_{02} = f_1 - f_2$, or is sideband coupled off the first mechanical resonance, $f_{02} = f_{01} + f_1 - f_2$. As before, this allows the simultaneous acquisition of the topographic imaging to take place on the fundamental resonance and the photo-induced force imaging to be detected on and amplified by the second mechanical resonance.

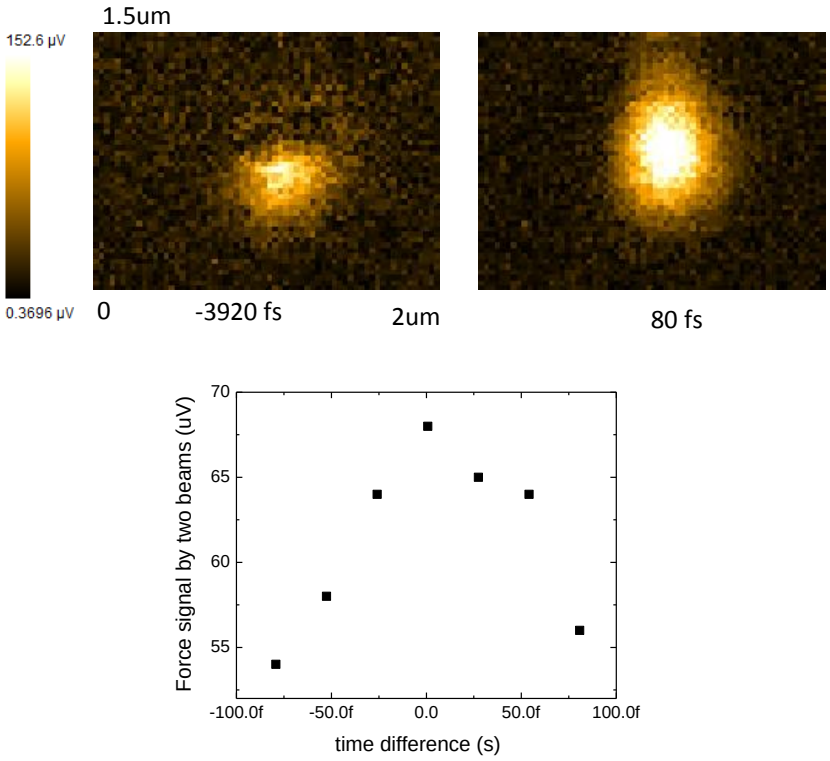

Figure 5.10 Tip scanned over the focal spot of two beams on plain glass substrate

The tip-scan over a fixed two-beam optical focus onto a glass substrate is shown in Fig. 5.10, here the nonlinear optical force is seen for a two-beam interaction at the difference frequency when the pulses are temporally overlapped, and when compared to the single beam profile in Fig. 3.3 the two-spot image is not apparent under these conditions. The cantilever characteristics on the first resonance were f_{01}=178 kHz, Q_1=490, and a stiffness constant k_1=58 N/m, and on the second resonance f_{02}=1098 kHz, Q_2=588, and k_2=2267 N/m, and operated with a free oscillation amplitude of A_{01}=47 nm.

The PiFM was then applied to investigate the pump-probe response of SiNc at the nanoscale. SiNc was spin cast as in section 2.3 into nanoclusters ranging from several micrometers to below 10 nm. The pump was tuned to 809 nm, near the linear absorption peak, and the probe to the peak of the excited state absorption spectrum at 605 nm. The amplitude modulation frequencies were set to f_1= 1000 kHz and f_2=2098 kHz so that $\Delta f = f_{02}$, overlapping the second mechanical resonance of the cantilever.

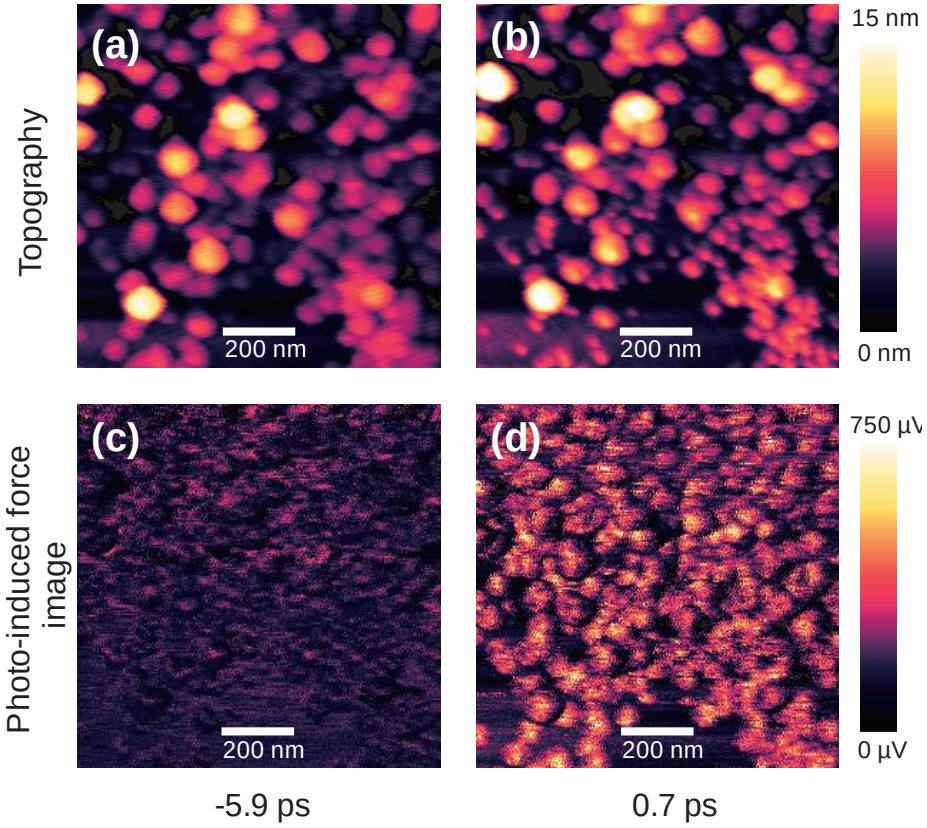

Figure 5.11 Negative probe timing topography a) and optical force c) simultaneously acquired; with positive pulse timing the optical force contrast d) is dramatically increased, while the topography b) is unchanged

In Fig. 5.11 topographic and photo-induced force images of SiNc nanoclusters are presented for two time delays between pulses, one where the probe was several picoseconds before the pump, and the other at positive-time near t0. The image is unchanged in the topographic channel with respect to pulse timing, but on the second resonance the photo-induced force images show little contrast during negative timing and then dramatic nanocluster contrast is seen on the excited state absorption peak with features as small as the tip curvature of ~10nm being resolved. As the gradient force is only dominant at very close nm distances and insensitive to volume effects the contrast in signal magnitude is quite uniform.

In Figure 5.12 a topographic and an optical force image are shown for another negative and positive-time image pair. Here, the topography images and the negative-time PiFM image show very little structural contrast while the positive-time optical force image shows dramatic nanocluster contrast. While the setup is optimized for measuring the optical force, we have seen other images (Fig 4.5) where the PiFM image provides greater contrast than the topographic image, which could be due to smaller clusters where the height is below the topographic noise floor, but due to the highly localized gradient force interaction and sensitivity can be still be seen through the optical force.

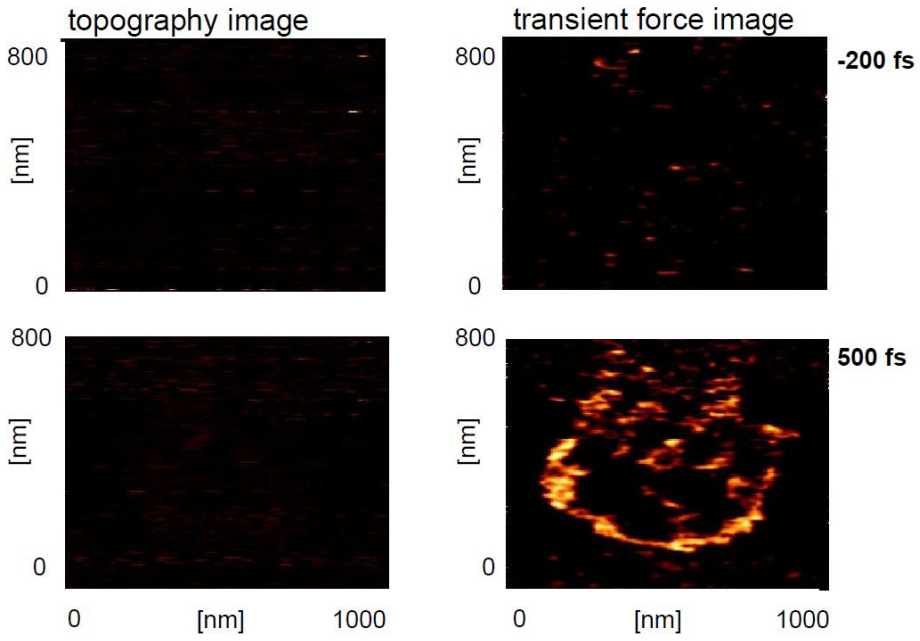

Figure 5.12 Topographic images at negative- a) and positive-time c) with no apparent structural contrast, optical force image demonstrates high contrast at positive-time d) where little was seen at negative-time b)

5.5 Time-resolved Pump-probe Force Microscopy

The use of nonlinear femtosecond excitation with the photo-induced force microscope can provide useful time-resolved information on the ultrafast dynamics of excitation and lifetime decay at the nanoscale. The non-optical detection sensitivity provided by PiFM opens possibilities for the time-resolved

study of a single chomrophore's excited state dynamics.

To extend the pump-probe PiFM imaging contrast into truly time-resolved information of the excited state decay dynamics images were taken at several time-delays.

In Figure 5.13 the pump-probe PiFM images of two SiNc nanoclusters are shown for various probe delays, providing time-resolved information about the lifetime of the S_1 excited state on the nano-scale. The time-delay dependence for decay of an excited state population is expected to be the same for PiFM pump-probe experiments as for optically-detected methods, since the dynamics in both pump-probe experiments are governed by excited state populations, and should then decay with τ_1.

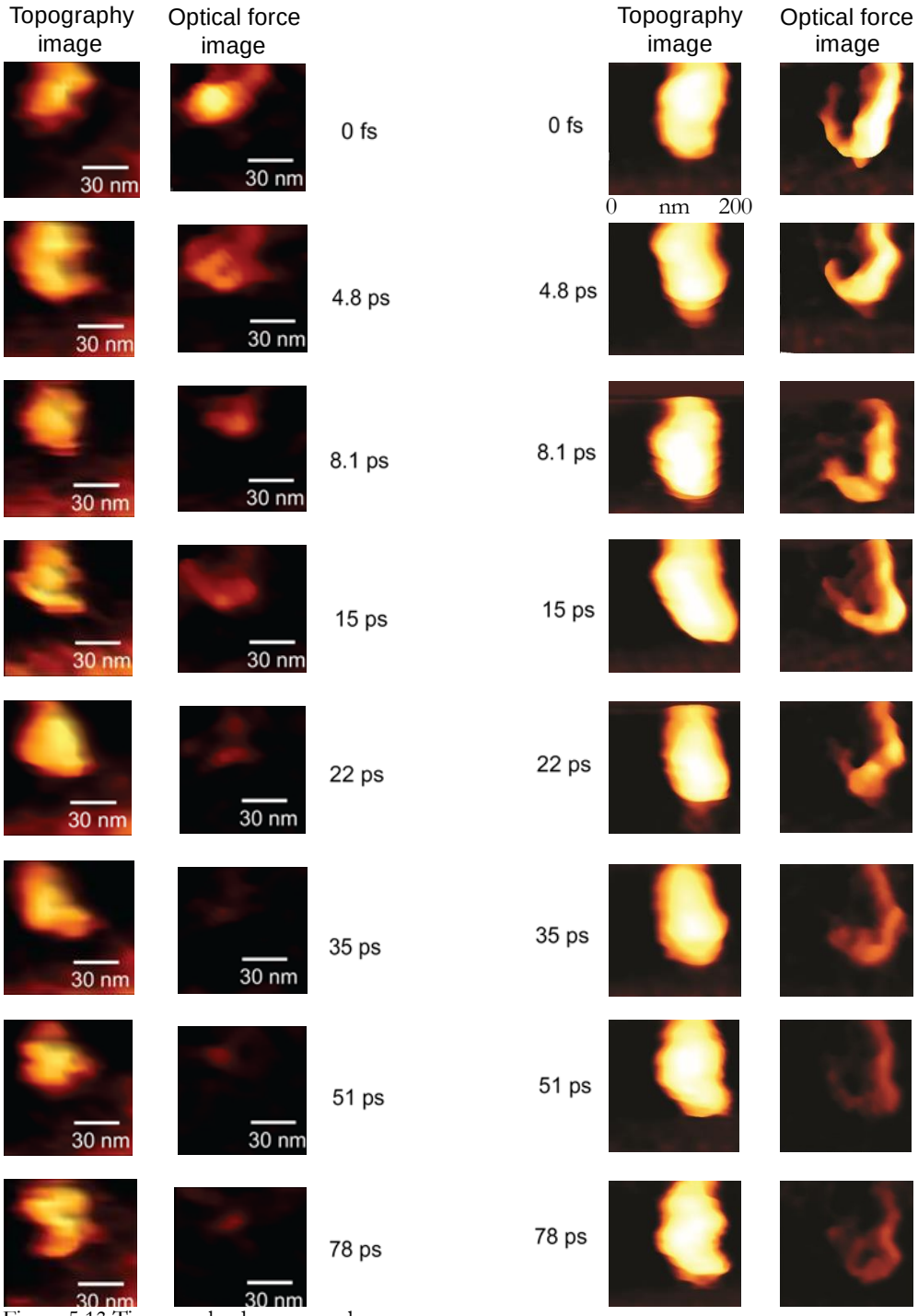

Figure 5.13 Time-resolved pump-probe PiFM for two SiNc nanoclusters, separated from the same image for clarity

In Figure 5.14 a direct comparison is made between the excited-state absorption dynamics for SiNc with completely optical detection on the microscopic scale and force detection by tr-PiFM images of nanoclusters. Here it is seen that both signals decay to the same dynamics as the system decays from the S_1 state with the approximately the same lifetime τ_1. This demonstrates that the PiFM technique is capable of interrogating the nonlinear optical properties of small quantities of molecules.

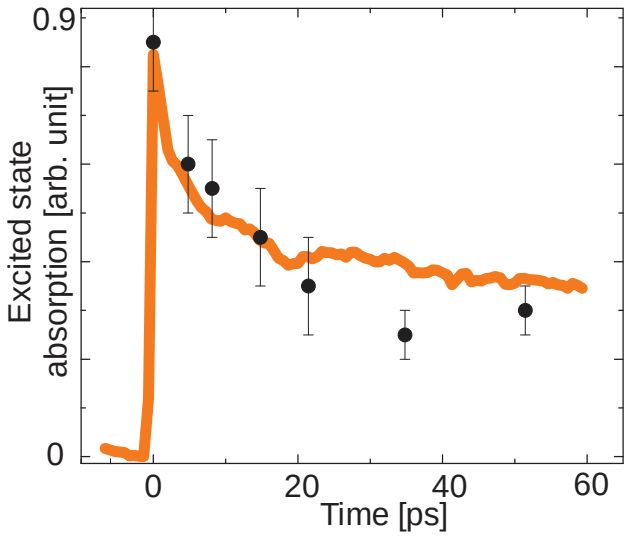

Figure 5.14 Comparison of excited state absorption dynamics for photodiode optical detection (orange line) and optical force detection (black circle dots)

Chapter Six

Conclusions

6.1 Summary

Previous photo-induced force microscopy experiments were done under CW illumination [40, 42]. The use of 200fs light pulses in this experiment is interesting because of several issues that may arise with the much greater peak powers when compared to cw illumination. Besides for the obvious potential photo-induced damage to the sample due to linear heating, optical nonlinearities at the tip could harm the stability of the experiment, especially since plasmon-resonances in the gold-coated tip can be excited by the 809nm wavelength used in our force-distance experiments [32, 61]. The strong fields then generated in the tip could cause nonlinear photodamage to the tip's structure, which changes the

tip's effective polarizibility. However we found that the use of a high repetition rate laser and average powers below 100 μW at the sample sustained stable imaging conditions for several hours.

The PiFM technique is directly sensitive to the electromagnetically induced forces in the tip-sample junction. As such it can operate in non-contact modes, unlike IR AFM techniques, and thermal expansion is not the primary contrast mechanism.

For single-beam studies it was shown that the contrast in linear photo-induced force microscopy is dictated by the spatial variation between two forces, the attractive gradient force, sensitive to the sample's polarizability and highly localized with a z^{-4} dependence, and the repulsive scattering force, an interaction between the excitation light and the tip. A theoretical description was provided of the cantilever dynamics in the presence of this optical force and the formulation developed allows for the reconstruction of the photo-induced forces from experimental amplitude-distance measurements.

The photo-induced force microscope probes various forms of optical transitions in chromophores by detecting the gradient force between the light-induced dipoles in tip and molecule. This extends to nonlinear optical excitations of the material, and we applied the PiFM to monitor the ultrafast excitation dynamics of SiNc at the nanoscale through non-optical detection. We demonstrated that time-resolved pump-probe force microscopy is sensitive to the same excited state absorption dynamics as far-field optical pump-probe measurements, with PiFM

signals from molecular assemblies as small as 10 nm, near the resolution of the microscope. The pump-probe force microscope benefits in sensitivity from the absence of a large optical background and further optimization could bring this technique to the limit of the single chromophore. The nonlinear PiFM technique can now be applied to a wide array of ultrafast spectroscopy studies at the nanoscale.

Bibliography

[1] W. Min, C.W. Freudiger, S. Lu, X.S. Xie, Coherent Nonlinear Optical Imaging: Beyond Fluorescence Microscopy, Annual review of physical chemistry, 62 (2011) 507-530.
[2] Image taken from http://hyperphysics.phyastr.gsu.edu/Hbase/phyopt/Raylei.html
[3] M. Orrit, J. Bernard, Single pentacene molecules detected by fluorescence excitation in a p-terphenyl crystal, Physical Review Letters, 65 (1990) 2716-2719.
[4] X.S. Xie, J.K. Trautman, Optical Studies of Single Molecules at Room Temperature, Annual review of physical chemistry, 49 (1998) 441-480.
[5] A. Gahlmann, J.L. Ptacin, G. Grover, S. Quirin, A.R.S. von Diezmann, M.K. Lee, M.P. Backlund, L. Shapiro, R. Piestun, W.E. Moerner, Quantitative Multicolor Subdiffraction Imaging of Bacterial Protein Ultrastructures in Three Dimensions, Nano Letters, 13 (2013) 987-993.
[6] W. Moerner, Single-Molecule Optical Spectroscopy and Imaging: From Early Steps to Recent Advances, in: A. Gräslund, R. Rigler, J. Widengren (Eds.) Single Molecule Spectroscopy in Chemistry, Physics and Biology, Springer Berlin Heidelberg, 2010, pp. 25-60.
[7] S.W. Hell, J. Wichmann, Breaking the diffraction resolution limit by stimulated emission: stimulated-emission-depletion fluorescence microscopy, Opt Lett, 19 (1994) 780-782.
[8] T. Watanabe, Y. Iketaki, T. Omatsu, K. Yamamoto, S.-i. Ishiuchi, M. Sakai, M. Fujii, Two-color far-field super-resolution microscope using a doughnut beam, Chemical Physics Letters, 371 (2003) 634-639.
[9] H. Okamoto, K. Imura, Near-field optical imaging of enhanced electric fields and plasmon waves in metal nanostructures, Progress in Surface Science, 84 (2009) 199-229.
[10] E. Ringe, B. Sharma, A.-I. Henry, L.D. Marks, R.P. Van Duyne, Single nanoparticle plasmonics, Physical Chemistry Chemical Physics, 15 (2013) 4110-4129.
[11] S.L. Kleinman, B. Sharma, M.G. Blaber, A.-I. Henry, N. Valley, R.G. Freeman, M.J. Natan, G.C. Schatz, R.P. Van Duyne, Structure Enhancement Factor Relationships in Single Gold Nanoantennas by Surface-Enhanced Raman

Excitation Spectroscopy, Journal of the American Chemical Society, 135 (2012) 301-308.
[12] J.A. Dieringer, R.B. Lettan, K.A. Scheidt, R.P. Van Duyne, A Frequency Domain Existence Proof of Single-Molecule Surface-Enhanced Raman Spectroscopy, Journal of the American Chemical Society, 129 (2007) 16249-16256.
[13] S. Yampolsky, D.A. Fishman, S. Dey, E. Hulkko, M. Banik, E.O. Potma, V.A. Apkarian, Seeing a single molecule vibrate through time-resolved coherent anti-Stokes Raman scattering, Nat Photon, 8 (2014) 650-656.
[14] Y. Jung, M.N. Slipchenko, C.H. Liu, A.E. Ribbe, Z. Zhong, C. Yang, J.-X. Cheng, Fast Detection of the Metallic State of Individual Single-Walled Carbon Nanotubes Using a Transient-Absorption Optical Microscope, Physical Review Letters, 105 (2010) 217401.
[15] T. Sheps, J. Brocious, B.L. Corso, O.T. Gül, D. Whitmore, G. Durkaya, E.O. Potma, P.G. Collins, Four-wave mixing microscopy with electronic contrast of individual carbon nanotubes, Physical Review B, 86 (2012) 235412.
[16] T. Kudo, H. Ishihara, Resonance optical manipulation of nano-objects based on nonlinear optical response, Physical Chemistry Chemical Physics, 15 (2013) 14595-14610.
[17] M.L. Juan, M. Righini, R. Quidant, Plasmon nano-optical tweezers, Nat Photon, 5 (2011) 349-356.
[18] P.C. Chaumet, A. Rahmani, M. Nieto-Vesperinas, Optical Trapping and Manipulation of Nano-objects with an Apertureless Probe, Physical Review Letters, 88 (2002) 123601.
[19] T. Kudo, H. Ishihara, Proposed Nonlinear Resonance Laser Technique for Manipulating Nanoparticles, Physical Review Letters, 109 (2012) 087402.
[20] L. Gross, F. Mohn, N. Moll, B. Schuler, A. Criado, E. Guitián, D. Peña, A. Gourdon, G. Meyer, Bond-Order Discrimination by Atomic Force Microscopy, Science, 337 (2012) 1326-1329.
[21] J. Zhang, P. Chen, B. Yuan, W. Ji, Z. Cheng, X. Qiu, Real-Space Identification of Intermolecular Bonding with Atomic Force Microscopy, Science, 342 (2013) 611-614.
[22] G. Binnig, C.F. Quate, C. Gerber, Atomic Force Microscope, Physical Review Letters, 56 (1986) 930-933.
[23] J.E. Sader, S.P. Jarvis, Accurate formulas for interaction force and energy in frequency modulation force spectroscopy, Applied physics letters, 84 (2004) 1801-1803.
[24] R. García, R. Pérez, Dynamic atomic force microscopy methods, Surface Science Reports, 47 (2002) 197-301.
[25] H.-J. Butt, B. Cappella, M. Kappl, Force measurements with the atomic force microscope: Technique, interpretation and applications, Surface Science Reports, 59 (2005) 1-152.

[26] C. Maragliano, D. Heskes, M. Stefancich, M. Chiesa, T. Souier, Dynamic electrostatic force microscopy technique for the study of electrical properties with improved spatial resolution, Nanotechnology, 24 (2013) 225703.
[27] V. Palermo, M. Palma, P. Samorì, Electronic Characterization of Organic Thin Films by Kelvin Probe Force Microscopy, Advanced Materials, 18 (2006) 145-164.
[28] A. Schwarz, R. Wiesendanger, Magnetic sensitive force microscopy, Nano Today, 3 (2008) 28-39.
[29] M. Pfreundschuh, D. Alsteens, M. Hilbert, M.O. Steinmetz, D.J. Müller, Localizing Chemical Groups while Imaging Single Native Proteins by High-Resolution Atomic Force Microscopy, Nano Letters, 14 (2014) 2957-2964.
[30] J. Bamidele, Y. Kinoshita, R. Turanský, S.H. Lee, Y. Naitoh, Y.J. Li, Y. Sugawara, I. Štich, L. Kantorovich, Chemical tip fingerprinting in scanning probe microscopy of an oxidized Cu(110) surface, Physical Review B, 86 (2012) 155422.
[31] M. Namboodiri, T. Khan, K. Karki, M.M. Kazemi, S. Bom, G. Flachenecker, V. Namboodiri, A. Materny, Nonlinear spectroscopy in the near-field: time resolved spectroscopy and subwavelength resolution non-invasive imaging, Nanophotonics, 3 (2014) 61-73.
[32] S. Berweger, J.M. Atkin, R.L. Olmon, M.B. Raschke, Light on the Tip of a Needle: Plasmonic Nanofocusing for Spectroscopy on the Nanoscale, The Journal of Physical Chemistry Letters, 3 (2012) 945-952.
[33] M.D. Sonntag, J.M. Klingsporn, L.K. Garibay, J.M. Roberts, J.A. Dieringer, T. Seideman, K.A. Scheidt, L. Jensen, G.C. Schatz, R.P. Van Duyne, Single-Molecule Tip-Enhanced Raman Spectroscopy, The Journal of Physical Chemistry C, 116 (2011) 478-483.
[34] T. Ichimura, S. Kawata, Surface- and Tip-Enhanced CARS, in: Surface Enhanced Raman Spectroscopy, Wiley-VCH Verlag GmbH & Co. KGaA, 2010, pp. 305-321.
[35] G.A. Hill, J.H. Rice, S.R. Meech, D.Q.M. Craig, P. Kuo, K. Vodopyanov, M. Reading, Submicrometer infrared surface imaging using a scanning-probe microscope and an optical parametric oscillator laser, Opt. Lett., 34 (2009) 431-433.
[36] A. Dazzi, C.B. Prater, Q. Hu, D.B. Chase, J.F. Rabolt, C. Marcott, AFM-IR: Combining Atomic Force Microscopy and Infrared Spectroscopy for Nanoscale Chemical Characterization, Appl. Spectrosc., 66 (2012) 1365-1384.
[37] C. Mayet, A. Dazzi, R. Prazeres, J.-M. Ortega, D. Jaillard, In situ identification and imaging of bacterial polymer nanogranules by infrared nanospectroscopy, Analyst, 135 (2010) 2540-2545.
[38] A. Dazzi, F. Glotin, R. Carminati, Theory of infrared nanospectroscopy by photothermal induced resonance, Journal of Applied Physics, 107 (2010) 124519.
[39] F. Lu, M. Jin, M.A. Belkin, Tip-enhanced infrared nanospectroscopy via molecular expansion force detection, Nat Photon, 8 (2014) 307-312.

[40] I. Rajapaksa, K. Uenal, H.K. Wickramasinghe, Image force microscopy of molecular resonance: A microscope principle, Applied physics letters, 97 (2010) 073121-073123.
[41] P. Saurabh, S. Mukamel, Communication: Atomic force detection of single-molecule nonlinear optical vibrational spectroscopy, The Journal of Chemical Physics, 140 (2014) -.
[42] I. Rajapaksa, H. Kumar Wickramasinghe, Raman spectroscopy and microscopy based on mechanical force detection, Applied physics letters, 99 (2011) 161103-1611033.
[43] L.H.B. Novotny, Principles of nano-optics, Cambridge University Press, Cambridge, 2012.
[44] R. Garcia, E.T. Herruzo, The emergence of multifrequency force microscopy, Nat Nano, 7 (2012) 217-226.
[45] J.N. Israelachvili, Intermolecular and surface forces / Jacob N. Israelachvili, Academic Press, London ; San Diego, 1991.
[46] J.E. Sader, T. Uchihashi, M.J. Higgins, A. Farrell, Y. Nakayama, S.P. Jarvis, Quantitative force measurements using frequency modulation atomic force microscopy—theoretical foundations, Nanotechnology, 16 (2005) S94.
[47] H. Urbach, S. Pereira, Focused fields of given power with maximum electric field components, Physical Review A, 79 (2009) 013825.
[48] G.R.J. Williams, Excited-state absorption and hyperpolarizability in silicon naphthalocyanines, Journal of Molecular Structure: THEOCHEM, 332 (1995) 137-140.
[49] E.J. Menke, M.A. Thompson, C. Xiang, L.C. Yang, R.M. Penner, Lithographically patterned nanowire electrodeposition, Nat Mater, 5 (2006) 914-919.
[50] D. Kleckner, D. Bouwmeester, Sub-kelvin optical cooling of a micromechanical resonator, Nature, 444 (2006) 75-78.
[51] J. Jahng, M. Lee, C. Stambaugh, W. Bak, W. Jhe, Active feedback cooling of massive electromechanical quartz resonators, Physical Review A, 84 (2011) 022318.
[52] L. Wei, W. Min, Pump-probe optical microscopy for imaging nonfluorescent chromophores, Analytical and bioanalytical chemistry, 403 (2012) 2197-2202.
[53] S. Chong, W. Min, X.S. Xie, Ground-State Depletion Microscopy: Detection Sensitivity of Single-Molecule Optical Absorption at Room Temperature, The Journal of Physical Chemistry Letters, 1 (2010) 3316-3322.
[54] M. Wagner, Z. Fei, A.S. McLeod, A.S. Rodin, W. Bao, E.G. Iwinski, Z. Zhao, M. Goldflam, M. Liu, G. Dominguez, M. Thiemens, M.M. Fogler, A.H. Castro Neto, C.N. Lau, S. Amarie, F. Keilmann, D.N. Basov, Ultrafast and Nanoscale Plasmonic Phenomena in Exfoliated Graphene Revealed by Infrared Pump–Probe Nanoscopy, Nano Letters, 14 (2014) 894-900.
[55] T. Guenther, C. Lienau, T. Elsaesser, M. Glanemann, V.M. Axt, T. Kuhn, S. Eshlaghi, A.D. Wieck, Coherent Nonlinear Optical Response of Single Quantum

Dots Studied by Ultrafast Near-Field Spectroscopy, Physical Review Letters, 89 (2002) 057401.
[56] K. Karki, M. Namboodiri, T. Zeb Khan, A. Materny, Pump-probe scanning near field optical microscopy: Sub-wavelength resolution chemical imaging and ultrafast local dynamics, Applied physics letters, 100 (2012) -.
[57] L. Wei, W. Min, Pump-probe optical microscopy for imaging nonfluorescent chromophores, Analytical and bioanalytical chemistry, 403 (2012) 2197-2202.
[58] W. Min, S.J. Lu, S.S. Chong, R. Roy, G.R. Holtom, X.S. Xie, Imaging chromophores with undetectable fluorescence by stimulated emission microscopy, Nature, 461 (2009) 1105-1109.
[59] D.D. Whitmore, Design and construction of linear and nonlinear optical systems for measurements of nanomaterials towards chemistry at the space-time limit, in, University of California, Irvine, Irvine, Calif., 2011.
[60] C.-Y. Chung, J. Hsu, S. Mukamel, E.O. Potma, Controlling stimulated coherent spectroscopy and microscopy by a position-dependent phase, Physical Review A, 87 (2013) 033833.
[61] M.I. Stockman, Nanofocusing of Optical Energy in Tapered Plasmonic Waveguides, Physical Review Letters, 93 (2004) 137404.